Investigations on the Design of the TACTIC Detector for the ^{8}Li(α,n)^{11}B Reaction

Thomas Kirchner

August 19, 2005

Investigations on the Design of the TACTIC Detector for the ^{8}Li(α,n)^{11}B Reaction

by

Thomas Kirchner[1]

Report on the Internship Term
(Praktisches Studiensemester)

at

TRIUMF
4004 Wesbrook Mall
Vancouver, BC V6T 2A3
Canada

Supervisors:

Prof. Dr. Günter Schatz[2] (Universität Konstanz)
Dr. Lothar Buchmann[3] (TRIUMF)

Universität Konstanz
Fachbereich Physik
Sommersemester 2005

[1]e-mail: thomas.kirchner@uni-konstanz.de
[2]e-mail: guenter.schatz@uni-konstanz.de
[3]e-mail: lothar@triumf.ca

Contents

List of Figures

List of Tables

Abstract

The ^{8}Li(α,n)^{11}B nuclear reaction is of importance in non-standard big bang nucleosynthesis models as well as for r-process nucleosynthesis. A new detector (TACTIC), designed to track and identify charged particles, is currently being developed to measure its cross section. In order to learn about the Gas Electron Multiplier (GEM), which will be one of its major components, and to measure the dependence of the signal gain on gas pressure and electric field conditions, a test setup was used. Efforts were made to improve the uniformity of the electric field in TACTIC and to calculate electron drift times. Using the GEANT4 package, a computer simulation was created, allowing the tracking of particles in TACTIC to be studied in more detail.

Chapter 1

Introduction

1.1 Nuclear Reactions in Astrophysics

1.1.1 The Origin of the Elements

One of the interesting challenges in astrophysics is to understand the creation of chemical elements in the universe and to explain their observed abundance. According to the standard big bang model of nucleosynthesis (SBBN), light nuclei were initially the only elemental matter in the universe. Hydrogen (about 75%) and helium (25%) nuclei were predominant, with small quantities of lithium isotopes. The synthesis of these nuclei takes place at temperatures around $T_9 \equiv T/10^9$ K $= 1$ [1]. When the temperature of a gaseous cloud drops below a point where the gravitational energy becomes larger than the thermal energy of its atoms (*Jeans criterion*), the cloud contracts, its interior heats up, and a new star is born. As soon as the temperature in the core reaches $T = 1.5 \times 10^7$ K, hydrogen burning can begin [2], provided the mass of the star is at least 1/10 of the solar mass [1]. Hydrogen burning results in a net conversion of four protons into a ^{4}He nucleus [3]:

$$4\mathrm{p} \longrightarrow {}^4\mathrm{He} + 2\mathrm{e}^+ + 2\nu, \quad Q = 26.73 \text{ MeV}$$

The Q value is the mass difference between the particles before and after the reaction. A positive value means that energy is released (*exothermic reaction*). As long as the hydrogen supply lasts, this energy output halts the gravitational contraction, allowing a star to shine continuously (*main sequence star*). By the time the supply of hydrogen is exhausted, the star will consist mainly of ^{4}He. After a phase of further contraction, and hence temperature increase, helium burning can start, producing elements like carbon and oxygen. Subsequent stages of stellar evolution include carbon, oxygen and neon burning as well as silicon burning. Nuclei up to a mass of 60 u can be formed in this way [1]. Eventually, in nova and supernova events, these heavy elements may be ejected and form interstellar clouds out of which new, second-generation stars can be formed.

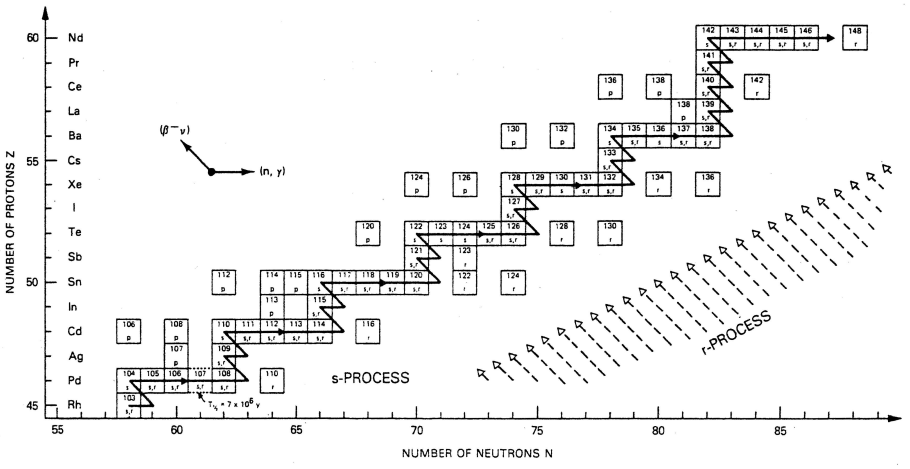

Figure 1.1: r- and s-process reaction paths in a section of the chart of nuclides. Taken from [1].

1.1.2 Synthesis of Heavy Nuclei

The probability for neutron-capture reactions is comparatively large for heavier nuclei [1]. It is most likely that the synthesis of heavy elements takes place in a neutron-rich environment by (n,γ) capture reactions, thus increasing the mass number by one

$$^{A}Z\,(\mathrm{n},\gamma)^{A+1}\,Z$$

until, in a step-by-step process, an unstable isotope is reached. Its β^--decay then leads to a new element $(Z+1)$. If neutron-capture occurs much more frequently than β-decay, this path is called the *r-process*. It is referred to as the *s-process* where the half-life is short compared to the time between successive neutron captures. The abundance of proton-rich nuclei, which obviously cannot be synthesized by the s- and r-processes, is smaller by two to three orders of magnitude [1], and they are believed to be created in a more complicated way (*p-process*).

1.1.3 Cross Sections and Reaction Rates

The probability for a reaction to occur is called the *total cross section* σ. For nuclear reactions, σ is typically of the order of 10^{-24} cm^2 = 1 b (barn). The reaction rate r for two particles x and y depends on their *relative* velocity v and on their spacial densities N_x, N_y and is given by [1]

$$r = N_x N_y \langle \sigma v \rangle \frac{1}{1+\delta_{xy}} \tag{1.1}$$

with the δ_{xy} term accomodating the possibility of reactions between two particles of the same kind. The angle brackets indicate the average over the velocity distribution $\Phi(v)$:

$$\langle \sigma v \rangle = \int_0^\infty \Phi(v) v \sigma(v) \mathrm{d}v \tag{1.2}$$

A Maxwell-Boltzmann distribution describes the velocities v_i of the nuclei $i = x, y$ [1]

$$\Phi(v_i) = 4\pi v_i^2 \left(\frac{m_i}{2\pi k_B T}\right)^{3/2} \exp\left(-\frac{m_i v_i^2}{2k_B T}\right) \tag{1.3}$$

where

$$\begin{aligned} m_i &= \text{mass of particle } i \\ k_B &= \text{Boltzmann constant} \end{aligned}$$

When tranformed into the center-of-mass system, one obtains [1]

$$\langle \sigma v \rangle = \sqrt{\frac{8}{\pi\mu}} \frac{1}{(k_B T)^{3/2}} \int_0^\infty \sigma(E) E \exp\left(-\frac{E}{k_B T}\right) \mathrm{d}E \tag{1.4}$$

with the c.m. energy $E = \frac{1}{2}\mu v^2$ and the reduced mass $\mu = \frac{m_x m_y}{m_x + m_y}$.

Theoretical and computational models of stellar evolution and nucleosynthesis rely on the nuclear reaction rates. It is the main task of experimental nuclear astrophysics to measure the energy dependence of the cross section.

1.1.4 Nonresonant Reactions

The rates of reactions involving two positively charged nuclei are mainly determined by their repulsive Coulomb force. It is the quantum mechanical tunnel effect that allows reactions to take place even below the Coulomb barrier energy E_C, albeit at much lower rates. The tunnelling probability depends sensitively on the energy and can, for $E \ll E_C$, be approximated by [1]

$$\sigma(E) \propto \exp(-2\pi\eta) \tag{1.5}$$

where η is the Sommerfeld parameter

$$\eta = \frac{Z_x Z_y e^2}{\hbar v} \tag{1.6}$$

and

$$\begin{aligned} Z_i &= \text{nuclear charge number} \\ \hbar &= \text{Planck's constant} \\ e &= \text{elementary charge} \end{aligned}$$

Furthermore, quantum mechanical considerations [1] suggest that the cross section is proportional to the square of the de Broglie wavelength λ of the $x + y$ two-particle system [4]

$$\sigma = \frac{1}{4\pi}\lambda^2 \quad \text{and} \quad \lambda \propto \frac{1}{\sqrt{E}} \tag{1.7}$$

The total cross section can then be expressed by

$$\sigma(E) = \frac{1}{E} \exp(-2\pi\eta) S(E) \tag{1.8}$$

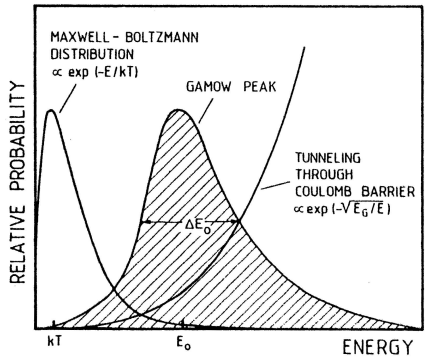

Figure 1.2: Typical progression of the cross section of a nonresonant reaction including the Gamow peak. Taken from [1].

where all purely nuclear effects are gathered in the *astrophysical S-factor* $S(E)$. Since the tunnelling probability drops so sharply with energy, cross section measurements at very low energies become increasingly difficult and eventually impossible to perform. Using the S-factor instead of the cross section allows for more accurate extrapolations to low energies, since for nonresonant reactions it varies smoothly with energy. Over a wide range, it can even be assumed constant $S(E_0)$. Then (1.4) becomes

$$\langle \sigma v \rangle = \sqrt{\frac{8}{\pi \mu}} \frac{1}{(k_B T)^{3/2}} S(E_0) \int_0^\infty \exp\left(-\frac{E}{k_B T} - \sqrt{\frac{E_G}{E}} \right) \mathrm{d}E \tag{1.9}$$

where E_G is the Gamow energy given by

$$E_G = 2\mu\pi^2 e^4 Z_1 Z_2 / \hbar^2 \tag{1.10}$$

Plotting equation (1.9) shows a peak (*Gamow peak*) around $E_0 = \left(\frac{\sqrt{E_G} k_B T}{2} \right)^{2/3}$. It is in this region that most nonresonant reactions involving charged particles occur, since the probability is highest there.

1.1.5 Resonant Reactions

When two particles react through a compound nucleus and the center-of-mass (c.m.) energy plus the Q value match one of the excitation energies E_x of the compound system,

$$E_x = E + Q \tag{1.11}$$

the cross section will, at that *resonance energy* $E = E_R$, be increased by several orders of magnitude [4]. Quantum mechanical selection rules decide whether or not a resonance can actually be observed. If the resonances are isolated (i. e., they do not overlap) and are sufficiently narrow, the Breit-Wigner formula holds [1]:

$$\sigma(E) = \frac{\lambda^2}{4\pi} \omega \tilde{\gamma} \tag{1.12}$$

ω is a statistical factor relating the number of states in the compound nucleus to the number of states in the entrance channel:

$$\omega = \frac{2J+1}{(2J_x+1)(2J_y+1)}(1+\delta_{xy}) \tag{1.13}$$

where

$$\begin{aligned} 2J+1 &= \text{number of magnetic sub-states for state with spin } J \\ J &= \text{spin of compound nucleus} \\ J_i &= \text{spin of reacting nuclei } i = x, y \end{aligned}$$

The resonance in the cross section can be treated as a harmonic oscillator swinging in an energy range $(E - E_R)$, giving rise to the oscillator term

$$\tilde{\gamma} = \frac{\Gamma_a \Gamma_b}{(E-E_R)^2 + (\Gamma/2)^2} \tag{1.14}$$

with

$$\begin{aligned} \Gamma_a \quad (\Gamma_b) &= \text{partial width of the formation (decay) of the compound nucleus} \\ \Gamma &= \Gamma_a + \Gamma_b \quad \text{(total width)} \end{aligned}$$

1.2 Kinematics of Nuclear Reactions

The cross section of a nuclear reaction depends only on the *relative* velocity of two reactants, so the movement of their center of mass is irrelevant for the reaction itself. Therefore, theoretical considerations are carried out in the c.m. system, whereas experimental observations are, of course, obtained in the laboratory system.

Consider a reaction

$$A + a \rightarrow B + b$$

and let a be the projectile, b the ejectile and B the recoil (see figure 1.3). The target nucleus A may be at rest in the lab system, i. e. its kinetic energy is $E_A = 0$. With $p_i = \sqrt{2m_i E_i}$, the conservation of momentum can be expressed in the following way:

$$\sqrt{2m_b E_b}\cos\vartheta + \sqrt{2m_B E_B}\cos\varphi = \sqrt{2m_a E_a} \tag{1.15}$$

$$\sqrt{2m_b E_b}\sin\vartheta - \sqrt{2m_B E_B}\sin\varphi = 0 \tag{1.16}$$

where m_i are the rest masses of the particles and E_i their kinetic energies in the lab frame[1]. Eliminating φ and inserting $E_B = Q - E_b + E_a$ yields the ejectile angle in the lab system:

$$\cos\vartheta = \frac{m_B\left(E_b\left(1+\frac{m_b}{m_B}\right) - E_a\left(1-\frac{m_a}{m_B}\right) - Q\right)}{2\sqrt{m_a m_b E_a E_b}} \tag{1.17}$$

[1] The non-relativistic energy-momentum-relation can be used here because at a maximum beam energy of about 1.5 MeV/u (see section 2.3) $v/c \approx 0.06 \ll 1$.

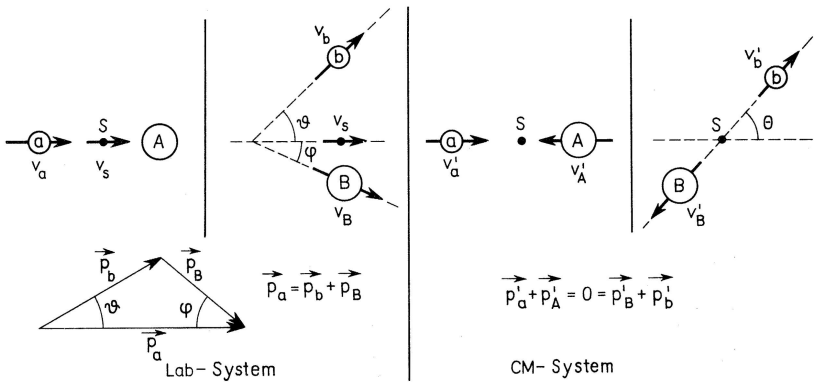

Figure 1.3: Kinematics of a nuclear reaction A + a $\rightarrow$ B + b in the lab system and in the c.m. system. Note that $\theta \equiv \vartheta^{\text{c.m.}}$. Taken from [2].

The ejectile's kinetic energy E_b depends on the ejection angle. It is calculated from [5]

$$E_b = f_1 + f_2 \cos\left(\vartheta^{\text{c.m.}}\right) \tag{1.18}$$

where [6]

$$f_2 = 2\frac{\sqrt{\mu_i E_i^{\text{c.m.}} \mu_f E_f^{\text{c.m.}}}}{M_A} \tag{1.19}$$

$$f_1 = f_3\left(E_b^{\text{c.m.}} + m_b\right) + E_b^{\text{c.m.}} \tag{1.20}$$

The c.m. energies in the entrance channel (i) and exit channel (f) are

$$E_i^{\text{c.m.}} = \frac{m_A}{m_a + m_A} E_a \tag{1.21}$$

$$E_f^{\text{c.m.}} = E_i^{\text{c.m.}} + Q \tag{1.22}$$

Reduced masses of entrance and exit channels:

$$\mu_i = \frac{m_a m_A}{m_a + m_A}, \quad \mu_f = \frac{m_b m_B}{m_b + m_B} \tag{1.23}$$

In the c.m. frame, the ejectile has the kinetic energy

$$E_b^{\text{c.m.}} = \frac{M_B}{M_b + M_B} E_f^{\text{c.m.}} \tag{1.24}$$

A relativistic correction is given by [6]

$$f_3 = \frac{M_a E_i}{\left(M_a + M_A\right) M_A} \tag{1.25}$$

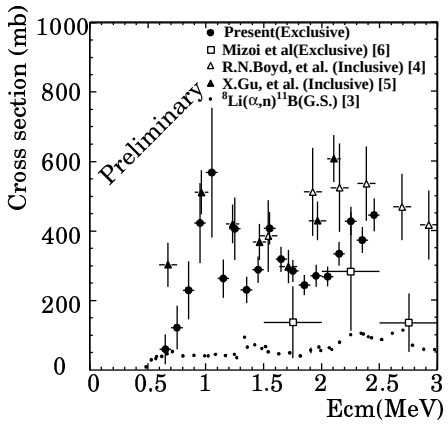

Figure 1.4: Previous measurements of the cross section of ^{8}Li(α,n)^{11}B. Figure taken from [8].

1.3 The ^{8}Li(α,n)^{11}B Reaction

It has been proposed [7] to design and implement a new detector, TACTIC (see sections 2.1 and 2.2), to measure the cross section for the ^{8}Li(α,n)^{11}B reaction due to its relevance to astrophysics. Results obtained in previous measurements of the cross section were far from consistent [8]. An approximate value for a ^{8}Li energy of 9 MeV is about σ = 400 mb, with roughly 1/5 resulting in the ^{11}B ground state and the rest in one of up to eight excited states [8].

1.3.1 Non-Standard Big Bang Nucleosynthesis

According to inhomogeneous big bang models of nucleosynthesis (IBBN), which differ from the standard model by the relaxation of the assumption of initial density uniformity, the synthesis of ^{12}C follows the pathway [7]

$$^{1}\mathrm{H(n,\gamma)}^{2}\mathrm{H(n,\gamma)}^{3}\mathrm{H(d,n)}^{4}\mathrm{He(t,\gamma)}^{7}\mathrm{Li(n,\gamma)}^{8}\mathrm{Li}(\alpha,\mathrm{n})^{11}\mathrm{B(n,\gamma)}^{12}\mathrm{B}(\beta\nu)^{12}\mathrm{C}$$

The ^{8}Li(α,n)^{11}B reaction faces the highest Coulomb barrier of this chain, and the half-life of ^{8}Li is only 840 ms; therefore, it is a crucial step in nucleosynthesis.

1.3.2 r-Process Nucleosynthesis

It is a condition for the synthesis of heavier elements that a sufficient number of seed nuclei be available. It has been believed that only heavy, iron-peak elements are of importance as seed nuclei. However, network calculations recently carried out by Terasawa et al. [9] suggest that reactions of light neutron-rich nuclei can influence the abundance predictions of heavier elements by a full order of magnitude. These calculations are based on supernova models assuming that conditions between the explosion shock-wave and the surface of the remaining core — a new neutron star — favour α particles and free neutrons over heavy nuclei, thus constituting an ideal environment for the r-process and α-capture

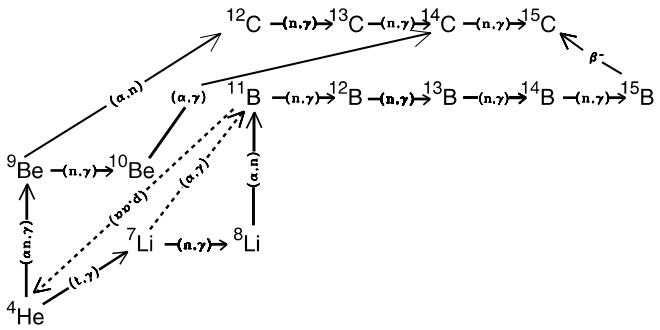

Figure 1.5: Reaction pathways leading to carbon isotopes. Figure taken from [9]

reactions (*α-process*). In the ealier stage of the explosion, the α-process is dominant, but it slows down as the temperature drops below about 2×10^9 K and then defers to the *r*-process.

One of the critical steps in seed nuclei breeding is ^{12}C. Under *r*-process conditions, the initial reaction pattern leading to ^{12}C changes considerably compared to the α-process environment. The Li-B chain is among those becoming most important in this case (see figure 1.5):

$$\alpha(\mathrm{t},\gamma)^7\mathrm{Li}(\mathrm{n},\gamma)^8\mathrm{Li}(\alpha,\mathrm{n})^{11}\mathrm{B}$$

Thus, the comparatively improbable three-body reaction $\alpha(\alpha\mathrm{n},\gamma)^9$Be can be bypassed. One of the key reactions to be investigated in order to allow estimates of the reaction flow is therefore ^{8}Li(α,n)^{11}B for which the TACTIC detector is primarily being developed.

1.4 Scope of the Work Carried Out

This report focuses on the work completed during a 20 week internship at the TRIUMF [10] facility. A brief outline of the TACTIC detector development project is given in chapter 2. It includes efforts put in developing the data acquisition in a test chamber setup (section 2.4), as well as measurements of the signal under varying conditions (section 2.5). Another main topic was the calculation of the electric field in the drift region of the proposed TACTIC detector to test several design options (section 3.2), and of a calibration curve for the derivation of ion tracks from the time signals (section 3.3). Finally, the basic features of a GEANT4 simulation of the detector were implemented (chapter 4).

Chapter 2

The TACTIC Chamber

2.1 TACTIC Layout

The TRIUMF Annular Chamber for the Tracking and Identification of Charged Particles (TACTIC), currently under development at the University of York (UK) and TRIUMF, is a combined ionization chamber and time projection chamber with a cylindrical design [11, 12]. An incident beam of ions runs into a gas filled target region along its rotation axis (z) where interactions with the gas target occur. Ejectiles are emitted into the drift region surrounding the target region, where, mainly by ionization of the drift gas, they gradually lose their kinetic energy and are eventually stopped. The electrons generated due to the ionization (δ-*electrons*) drift towards anode strips situated on the inside of the cylinder barrel, their drift time indicating the location of their production. The arrangement envisioned includes 48 annular copper anode ring pads along the z axis printed onto a G10 plate. An azimuthal subdivision is also conceivable; it is vital in case the chamber is used for reactions involving high anode counting rates exceeding the readout speed of a single strip. Also, if the distribution of ejectiles is expected to be asymmetric, e. g. in possible experiments with polarized beams, the φ information must be obtained. Otherwise the cylindrical layout takes advantage of the rotational symmetry. Another possible approach

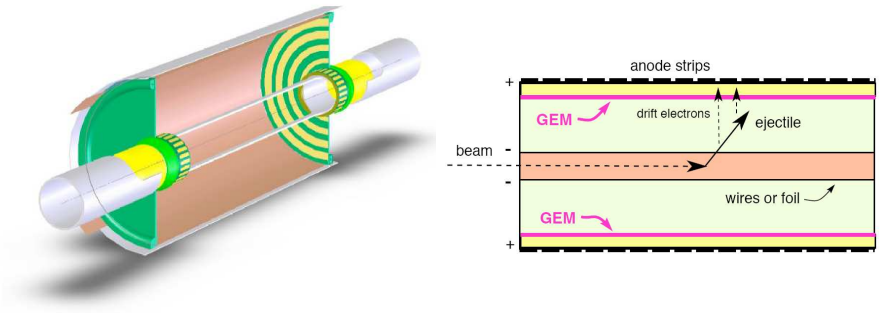

Figure 2.1: Three-dimensional cut-away view (left) and schematic side view (right) of the TACTIC detector chamber. Taken from [11].

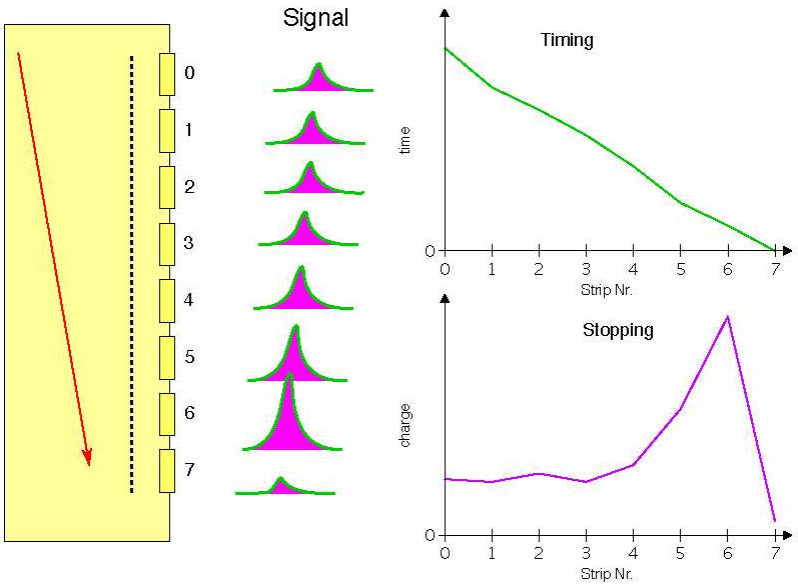

Figure 2.2: A schematic diagram showing signals from TACTIC's anodes allowing the tracking and identification of charged particles. Here, time is with respect to the last anode. Taken from [12].

to determine the azimuth coordinate is using backgammon-type anodes as described in ref. [13].

The cathode is formed by a separating foil between the target and drift regions, or by using an array of cathode wires, depending on the application of the chamber. In the latter case, of course, both the target and the drift region must be filled with the same gas. It has been shown [11] that a cage of appropriately biased additional wires, at a slightly smaller radius than the cathode wires, collects all beam electrons; thus they are prevented from entering the drift region.

The charge collected by the anodes depends on the energy loss (the stopping power $\mathrm{d}E/\mathrm{d}x$) of the ejectiles, by which means it is possible to identify the ejectile species. The time signals of the arrival of the δ-electrons at consecutive anodes enable the determination of the particle trajectory, if the electron drift velocity is taken into account. As will be shown, the electron drift time is of the order of μs, i. e. slow compared to the passage of the ion.

A first stage of charge signal amplification is provided by a Gas Electron Multiplier (GEM) [14] placed at a short distance from the anode pads. Essentially, a GEM is a flexible 50 μm foil of isolating material with thin conducting layers on either side between which a high voltage is applied. There are holes with a diameter of 50 μm and 150 μm pitch through which electrons can travel. The strong local electric field causes them to multiply by the avalanche effect. Therefore, only one further stage of signal amplification is required, which is provided by a preamp board.

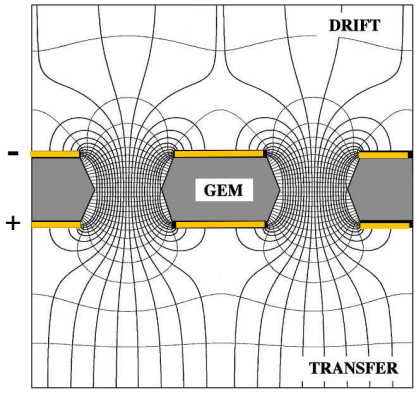

Figure 2.3: The electric field leading to electron signal amplification at a GEM. Figure taken from [12].

The data aquisition (DAQ) comprises 48-channel flash-ADC boards, sampling the shape of the pulses delivered through the preamplifiers. Moreover, the flash-ADC takes care of the time and charge information extraction. The software part of the DAQ is taken on by a MIDAS [15] system, with ROME [16] acting as a convenient interface between MIDAS and ROOT [17]. The latter is a standard package for data analysis widely used in nuclear physics.

2.2 Application

The first nuclear reaction to be measured in TACTIC will be ^{8}Li(α,n)^{11}B, in the c.m. energy range of 0.4 to 3 MeV. This corresponds to a ^{8}Li beam energy of 0.15 to 1.13 MeV/u. Higher beam intensities (up to 10^{7} pps) can be used than in previous experiments [7] since beam particles are not tracked, thanks to the separation of target and drift region. The target gas in this instance is helium. By using the same gas for detector and target, TACTIC can be operated in a windowless mode, i. e. with cathode wires rather than a separating foil. By this means, the energy attenuation of the ejectiles can be eliminated. CO_2 is added as a quenching gas in order to suppress photons resulting from atomic excitation. Tests performed at a test chamber (see section 2.4) yielded the highest signal amplification when the He/CO_2 ratio was 90%/10% [11].

The main source of background is elastic scattering, however, since scattered α particles will be in coincidence with elastic ^{8}Li, and the ^{8}Li energy loss differs significantly from ^{11}B, these events can be discriminated from the desired reactions. Mounting an array of bismuth germanate (BGO) scintillation detectors around the TACTIC chamber allows for the detection of γ events from excited states of the reaction product. This provides a coincidence signal giving further indication of whether or not an event is to be considered.

Another proposed reaction is ^{7}Be+p elastic scattering [18], for which a hydrogen gas target is needed. The drift region will then be separated by a thin foil. This option, however, will not be discussed in this report.

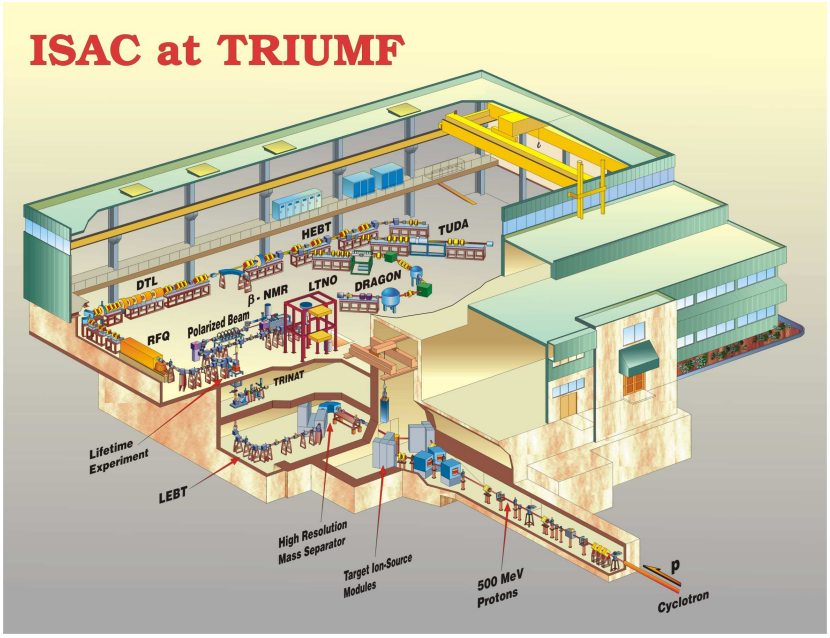

Figure 2.4: The ISAC facility at TRIUMF. Figure taken from [19].

2.3 The ISAC Facility at TRIUMF

At the end of 2005 or early in 2006, a TACTIC prototype is scheduled to be assembled and mounted on a beam line of the Isotope Separator and Accelerator (ISAC) [19] at TRIUMF. This facility is capable of delivering beams of radioactive ions with masses up to 30 u and energies between 0.153 and 1.53 MeV/u. A 500 MeV proton beam accelerated in the TRIUMF main cyclotron is used to produce a variety of nuclei when steered onto an ISAC target. A mass separator allows the choice of one particular ion species with high precision from those extracted from the ion source. For the nuclear astrophysics experiments, a pulsed structure is imposed on the beam by a pre-buncher, a radio frequency quadrupole (RFQ) and several subsequent bunchers. The drift tube linac (DTL) then accelerates the beam to its designated energy, and the high energy beam transport system (HEBT) takes it to either the DRAGON [20] or TUDA [21] experiment.

2.4 The Test Chamber

2.4.1 The Setup

A planar test chamber serves as a setup to investigate the gas mixture, the pressure and field dependence of the signals, and to test the DAQ. The test chamber drift volume is about 20 × 20 cm with a height of 2 cm. A GEM foil mounted 3 mm above the 5 mm anode strips covers an active detection area of 8 × 8 cm, i. e. 16 anodes can be used. GEM and anodes are fed by a common power supply with the voltage ratio being fixed to 3.3. An HV board,

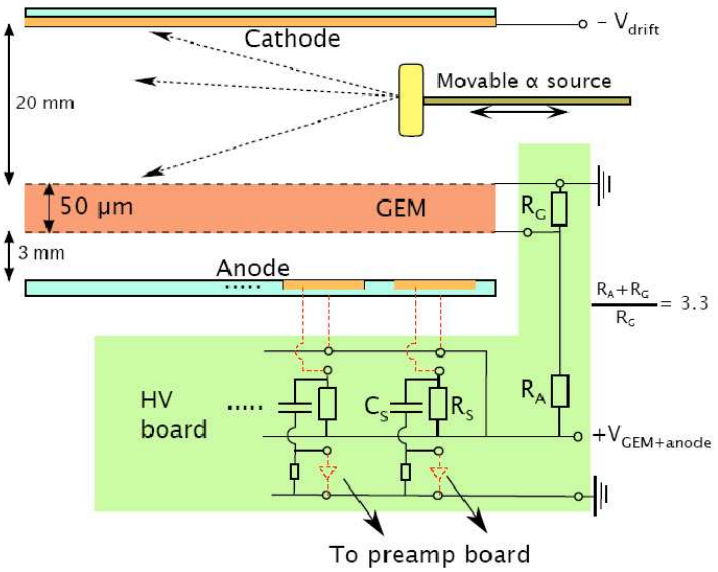

Figure 2.5: Schematic view of the TACTIC test chamber. Typical operation parameters are $V_{\text{drift}} = 500$ V and $V_{\text{GEM+anode}}$ between 900 V and 1500 V, depending on the gas pressure [22]. Usually, the chamber is operated at gas pressures between 100 mbar and atmospheric pressure.

which also comprises this voltage divider, decouples the anode signals. Events are generated by a ^{241}Am α source (5.486 MeV), movable perpendicular to the anode strips. A 16 μm thick Mylar foil covers the front of the source, leading to directional straggling of the α particles as well as to an energy reduction. An external gas handling system keeps the gas mixture at 90/10 He/CO_2 with a flow of about 200 cm^3/min.

2.4.2 Data Acquisition

Previous applications of the test chamber include investigations of the signal dependence on the GEM+anode voltage and the gas mixture and pressure. Moreover, the voltage range in which the GEM is operational with the signals being distinguishable from background noise, was established [11].

In order to allow for the simultaneous observation of signals from up to four consecutive anode strips, an analogue electronics setup was assembled as shown in figure 2.6. The inputs are positive signals delivered by the HV board and a subsequent four channel preamplifier board (see figure 2.7).

For further processing[1], the signals need to be inverted and amplified, before being fed into a peak-sensing analogue-digital converter (ADC) which digitizes the signal size. On top of that, a time-digital converter (TDC) is used to extract the time information from logical pulses. The latter are generated by a constant fraction discriminator (CFD), triggering a logical timing signal as soon as the

[1] At the time of writing, the flash-ADC board available was not yet operational.

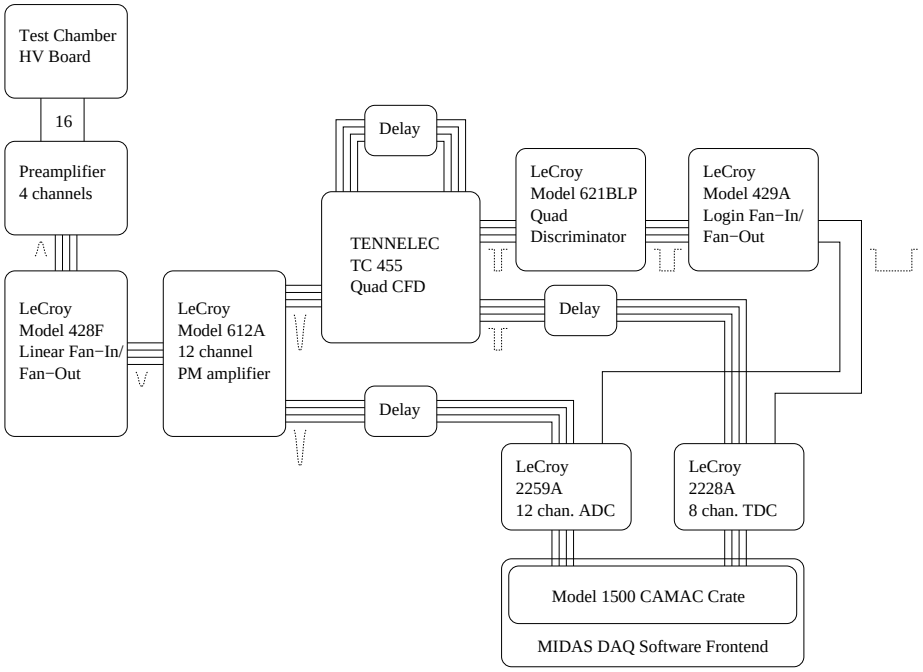

Figure 2.6: The DAQ analogue electronics at the TACTIC test chamber. Typical pulse shapes after each module are indicated in dashed print.

original signal has risen to a certain fraction of its peak amplitude (see figure 2.8). After that, the pulses are shaped allowing the signals from four channels to overlap, so that subsequently, the shaped pulses can be processed by a logical OR to produce the required ADC and TDC gates. The ADC and TDC modules are mounted in a CAMAC crate connected to a PC, on which the MIDAS DAQ software frontend runs. The data processing is accomplished by ROME and ROOT.

From figure 2.7 it can be seen that the signal shape of the first channel differs from the others. This problem is due to a defect in the preamp board. Therefore, only the other three channels can be used when analysing the data.

As the electronics upgrade neared completion, the GEM foil suddenly failed. It was removed from the chamber, but could not be reused even after repeated attempts to clean it using an ultrasonic bath. Inspection under a microscope did not reveal evidence of physical damage. However, as soon as the chamber was reassembled, the resistance between the two conducting layers persisted to drop to a few kΩ, where at least several GΩ would be expected. All GEM handling was performed at clean room conditions. Eventually, in order to make the chamber operational, a new GEM foil had to be built in.

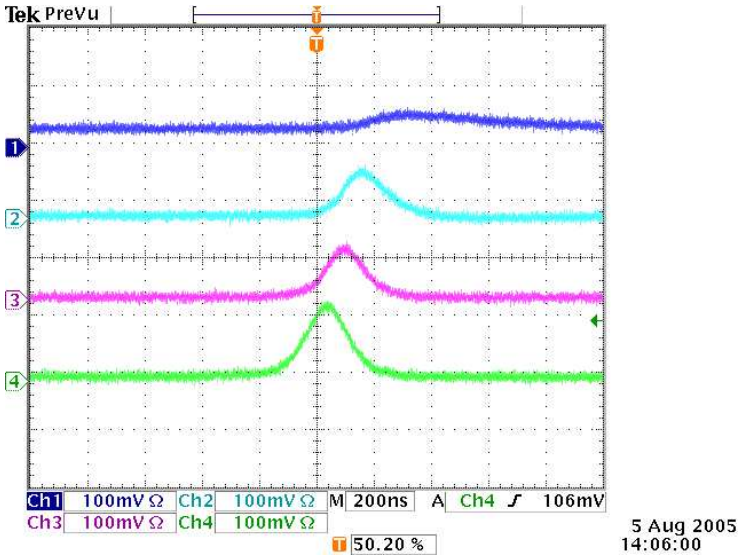

Figure 2.7: Oscilloscope screenshot: single event preamplified signals from 4 successive anodes (GEM+anode voltage = 1400 V, pressure = 1000 mbar). The shape of the signal on the first channel is due to some defect in the preamp board.

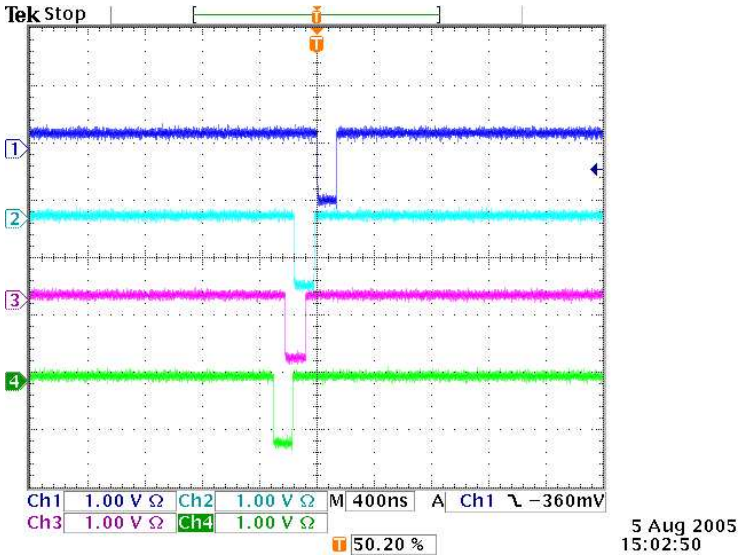

Figure 2.8: Oscilloscope screenshot: single event locigal time signals (after CFD) from 4 successive anodes (GEM+anode voltage = 1300 V, pressure = 1000 mbar).

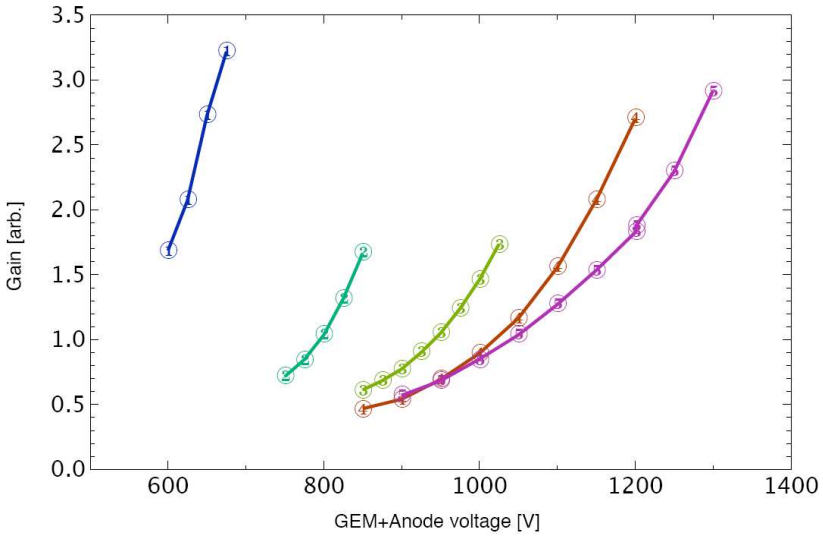

Figure 2.9: Relative signal gain provided by the test chamber GEM for low gas pressures. Numbers in the circles represent the pressure in mbar, divided by 100. Taken from [22].

2.5 GEM Signal Gain

Clearly, the signal gain factor produced by the GEM depends on the applied voltage, and also on the gas pressure. Previous measurements [22] resulted in the data shown in figure 2.9, covering the low-pressure range from 100 mbar to 500 mbar. With the improved DAQ electronics described in section 2.4.2, these findings were complemented by measurements extending from 500 mbar to 1000 mbar. The approach chosen was to take ADC spectra of the second channel (the first one was not used due to the defect in the preamp board) at a constant α source distance of 45 mm from the corresponding anode strip. Refer to appendix A.1 for an overview of the data taken and to appendix A.2 for a listing of the spectra obtained.

As expected, the ADC signal height is larger with higher voltages, resulting in a shift of the histogram peak to higher channels. For every pressure step, the spectra taken at different GEM+anode voltages were scaled to visually match the one at 1200 V[2] according to

$$\text{histogram}_{\text{scaled}}[i] = \text{histogram}[i/s_V]/s_V$$

where histogram$[i]$ represents the number of events registered at the i-th histogram channel. To account for the difference in initial ionization and pressure, the scaling factors s_p [6] for the matching of simulated spectra at different gas pressures to the one at 1000 mbar were used. They are given in table 2.1 and were multiplied by the parameters obtained for the experimental data, normalizing all data to 1000 mbar and 1200 V. A gain factor in arbitrary units is then

[2]Note that the GEM voltage is by a factor 3.3 smaller than the GEM+anode voltage.

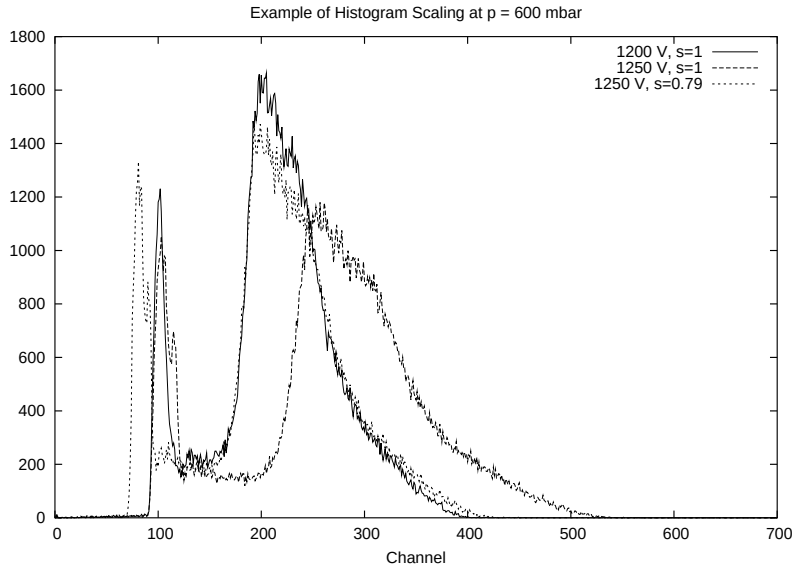

Figure 2.10: Example of ADC spectra and the scaling procedure. The very sharp peak around channel 100 is background noise.

Gas pressure [mbar]	s_p
100	0.08
200	0.16
300	0.25
400	0.34
500	0.43
600	0.53
700	0.64
800	0.75
900	0.88
1000	1

Table 2.1: Scaling factors obtained from simulated spectra for different gas pressures [6]. See text for further explanation.

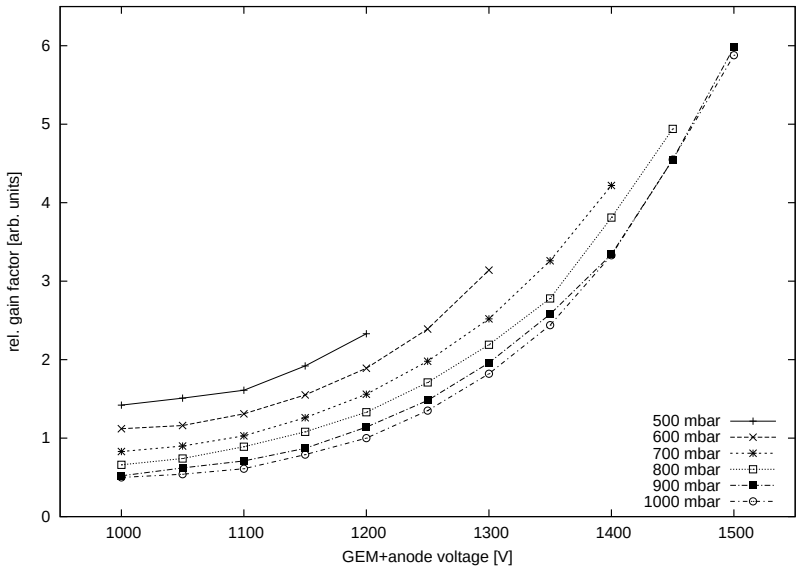

Figure 2.11: Relative signal gain $1/s_V s_p$ provided by the GEM. The upper end of each curve is just short of the pressure-dependent breakdown voltage of the GEM. The lowest one or two data points of each curve are less reliable due to a drop in the counting rate, see appendix A.1.

given by

$$\text{gain} = \frac{1}{s_V s_p}$$

The error on this rather crude procedure is estimated to be approximately 10% and represents the uncertainty in visually matching a scaled histogram to another one. The results are summarized in tables A.1 and A.2, and the corresponding curves are shown in figure 2.11. Note that the values also contain the signal amplification due to the electronics.

Chapter 3

Electrons in the TACTIC Drift Region

3.1 Motivation

For the deduction of the ejectile tracks from the anode time-of-flight (TOF) signals it is crucial to know the electron drift velocity in the gas mixture used, which strongly depends on the local electric field strength. Therefore, the field in the TACTIC drift region must be known as accurately as possible. Since the enclosure behind the end caps must be electrically grounded to provide shielding against the outside environment, the field will be distorted near the ends, as compared to the ideal field that would be found in the interspace between two concentric charged cylinders (ideal electric conductors) of infinite length. The latter can be calculated using Gauss' law

$$\nabla \vec{D} = \rho \tag{3.1}$$

where $\vec{D}$ denotes the electric displacement field and ρ the electric charge density. Equation (3.1) is integrated over a concentric cylindrical volume of the length l and radius r with $R_1 < r < R_2$, where R_1 is the radius of the inner cylinder, and R_2 the radius of the outer one. With q denoting the electric charge line density enclosed by the integration volume and $\mathrm{d}\vec{s}$ a surface vector element, this yields:

$$q \cdot l = \int_V \nabla \vec{D} \mathrm{d}V = \oint_{\partial V} \vec{D} \mathrm{d}\vec{s} = D_r \cdot 2\pi r \cdot l$$

Furthermore, assuming the material between the two cylinders to be dielectric, the electric field, which points in the radial direction, is found to be proportional to r^{-1}. Thus, the electric potential is

$$V(r) = \alpha \ln \frac{r}{\beta} \tag{3.2}$$

with the constants α and β being determined by the boundary condition $V(R_1) = V_1$ and $V(R_2) = V_2$ to adhere to

$$\begin{aligned} \frac{1}{\alpha} &= \ln\frac{R_2}{R_1}\cdot\frac{1}{V_2 - V_1} \\ \frac{1}{\beta} &= \frac{1}{R_1}\exp\left(\frac{V_1}{V_2 - V_1}\cdot\ln\frac{R_2}{R_1}\right) \end{aligned}$$

The charge line density is also determined by the above conditions but of no interest in this context.

3.2 Improving the Field Uniformity

3.2.1 The Femlab Package

In order to calculate the electric potential distribution in the proposed TACTIC configuration, it is necessary to take into account the actual geometry in more detail. Due to its complexity, an analytic approach is not feasible. Instead, a numerical method, the Finite Element Method (FEM), is employed.

FEMLAB[1] [23, 24] is a FEM software package that allows for the specification of a geometry in up to three space dimensions, as well as its properties, which will depend on the physics mode used. In this instance, FEMLAB is used in the 3D electrostatics mode. The voltages applied to surfaces can be specified, as well as the dielectric permittivity of subvolumes. Output of the results is provided in the form of various plot options, including the potential distribution and the electric field lines. Additionally, FEMLAB allows for external analysis of the data by printing the resulting values to file.

3.2.2 Femlab Models

In an effort to contain the calculation time and memory consumption to be manageable by a standard desktop PC[2], the FEMLAB models of the TACTIC drift region were designed to feature only the amount of complexity needed for the purpose of calculating the said fringe effects on the electric field. The cathode wires were replaced by a simple cylinder with radius $R_1 = 10$ mm, and the GEM was omitted. The radius of the outer cylinder representing the anode surface was chosen to be $R_2 = 50$ mm. A voltage of -500 V is applied to the cathode, and ground to the anode. The tube, which extends to a length of 20 cm, is enclosed at the top and bottom by 2 mm thick end caps consisting of a dielectric ($\varepsilon_r = 10$). The enclosure, which has ground potential, is placed 10 mm behind them. Thin ring structures carrying potentials U_i, that follow the logarithmic progression (3.2), are added on the inside face of the caps. Configurations with three, six, and nine ring pads have been investigated and compared to one without any pads. The exact specifications are given in appendix B.1. Note that, taking advantage of the symmetry, the calculations for the six- and

[1] Version 3.1

[2] The machine used throughout most of the work presented in this report runs Linux and features a 1.3 GHz single processor and 512 MB of RAM. Plenty of swap memory (3 GB) was allocated to accomodate FEMLAB.

nine-ringed models are based on one half of the cylinder only. From the voltage distributions obtained (see figure 3.1) one can immediately find that appropriately biased end cap rings support the electric field at the edges, thus helping to improve the field uniformity.

3.2.3 Tracking Algorithm

In order to further assess and quantify the uniformity of the electric field obtained, the drift time of electrons when travelling from the cathode to the anode was calculated, as well as the maximum deviation Δz of field lines from their starting height.

FEMLAB provides the E_x, E_y, and E_z components of the resulting electric field at equidistant grid points, along with the cartesian coordinates of these grid points. The z axis points along the rotational symmetry axis with the two end caps placed at $z = 0$ m and $z = 0.2$ m. In this instance, only the data in the $y = 0$ plane were used, taking advantage of the rotational symmetry of the problem. The following loop algorithm was implemented in C++ (see appendix B.2) to track the field lines and to calculate their maximum deviation Δz from their starting point ($x_{\text{start}} = R_1$, $y_{\text{start}} = 0$, z_{start}), as well as the electron drift time along the field lines:

1. E_x and E_z take the values given for the closest grid point[3].
2. The width δx of a step in x direction is kept at the constant x distance between grid points, and $\delta z = (E_z/E_x)\,\delta x$.
3. The drift time is increased by $\sqrt{\delta x^2 + \delta z^2}/w(|\vec{E}|)$, where w denotes the drift velocity of an electron approximated from experimental data [25] to $w(E) = 0.9 \text{ m s}^{-1}/\text{V m}^{-1}$ (see figure 3.3).
4. x and z are increased by δx and δz, respectively.
5. Remember $\Delta z = |z_{\text{start}} - z|$ if it is larger than any Δz previously obtained.
6. Go to 1.

This loop will be executed while $R_1 < x < R_2$ and $0 < z <$ length of the chamber.

3.2.4 Results

Refer to figures 3.4 and 3.5 for plots of the results. They show that, in order to reduce the fringe effect caused by the end caps of the TACTIC drift region, it is desirable to install annular conducting ring pads on the end caps. If the voltages applied to them fit the logarithmic progression of the potential, the influence of only three pads is sufficient to considerably improve the uniformity of the electric field, thus increasing the sensitive detection area. Additional pads have slighter effects.

[3]It has not been deemed necessary to provide for interpolation. Since the number of grid points can be increased virtually arbitrarily, this task can be left to FEMLAB.

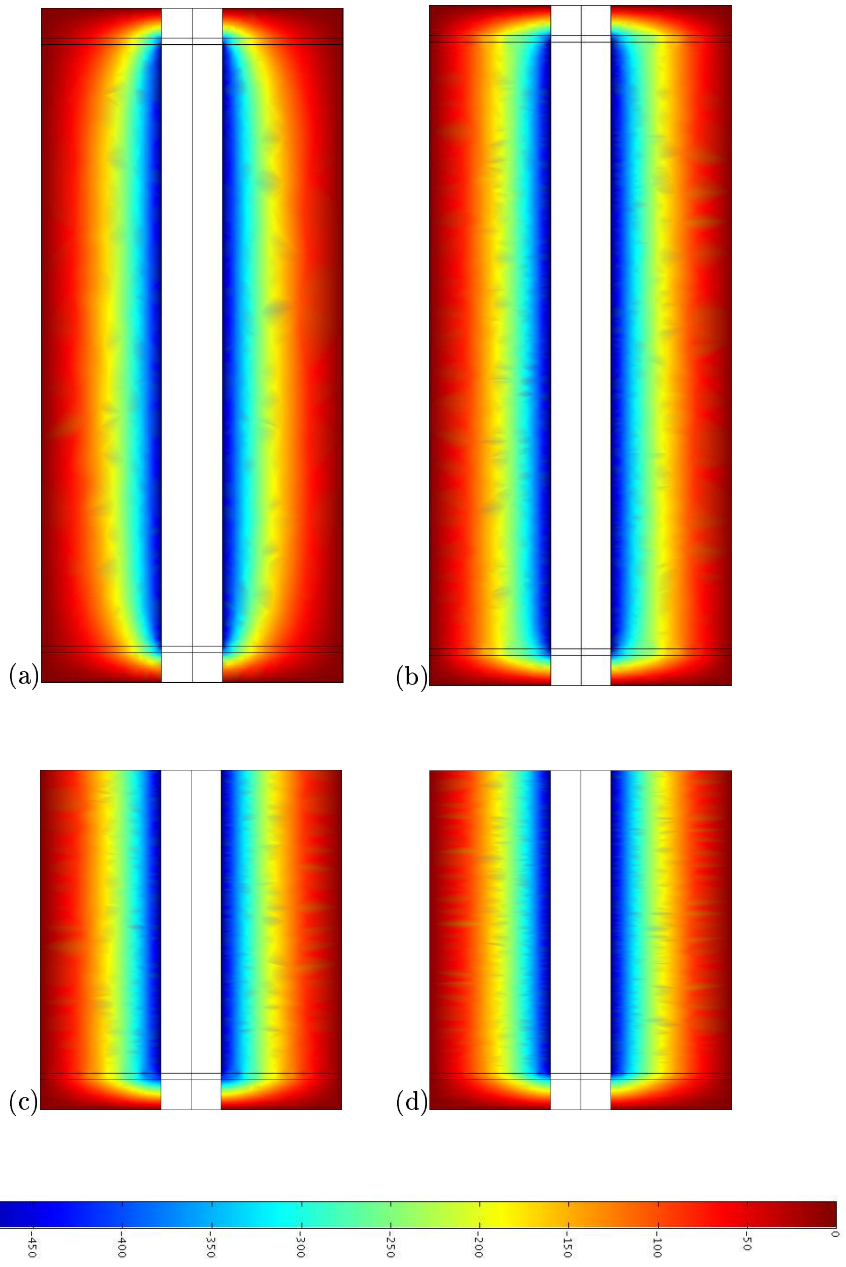

Figure 3.1: The resulting voltage distribution with (a) no rings, (b) 3 rings, (c) 6 rings, and (d) 9 rings to support the electric field at the end caps. Key units are volts.

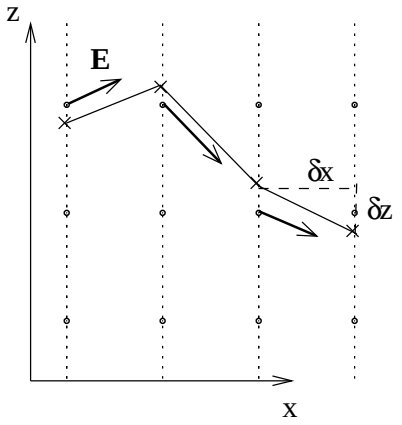

Figure 3.2: The field line tracking algorithm. The dots shown are the grid points where $\vec{E}$ values are available (arrows). δx and δz denote the width of a step in x and z direction, respectively. The solid line indicates the field line found.

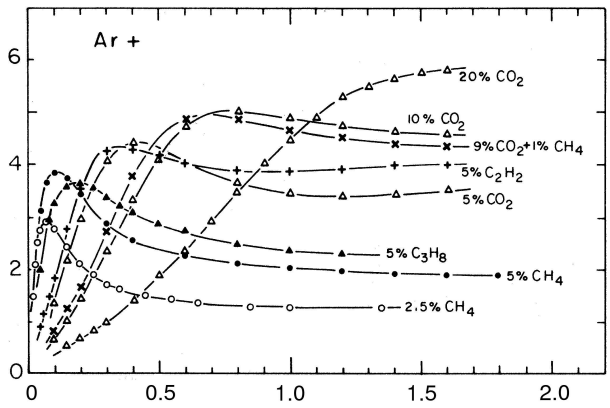

Figure 3.3: Drift velocity $w(E)$ of e^- in an Ar/CO_2 gas mixture, taken from [25, figure 63]. The abszissa quantity is E/p in kV/cm/atm, and the ordinate is $w(E)$ in cm/μs. The 10% CO_2 curve in the range $E < 500$ V/cm at atmospheric pressure is approximately $w(E) \approx 0.9$ m s^{-1}/V m^{-1} .

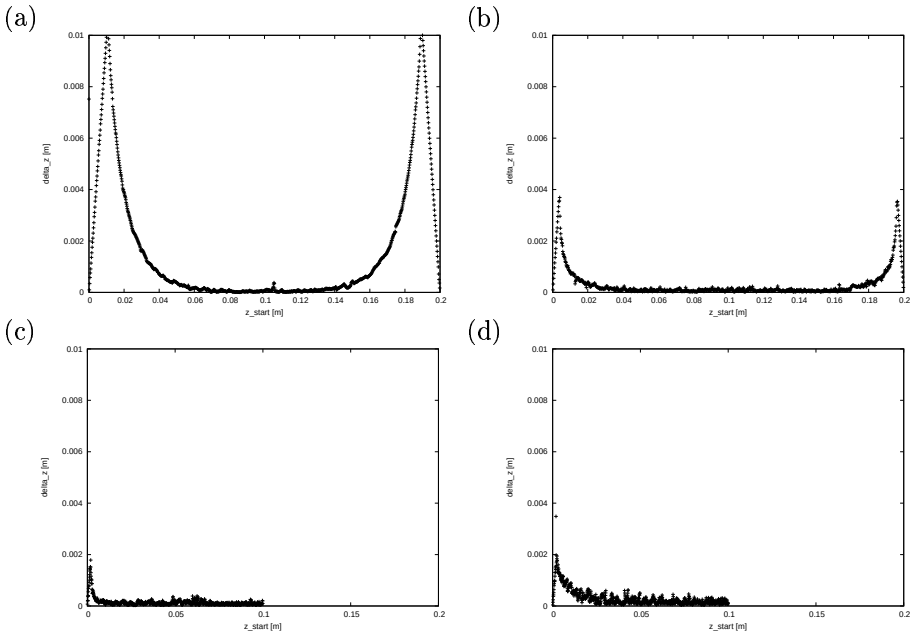

Figure 3.4: The maximum deviation Δz of field lines from their starting point at z_{start} in the FEMLAB models as a function of z_{start} with (a) no rings, (b) 3 rings, (c) 6 rings, and (d) 9 rings to support the electric field at the end caps

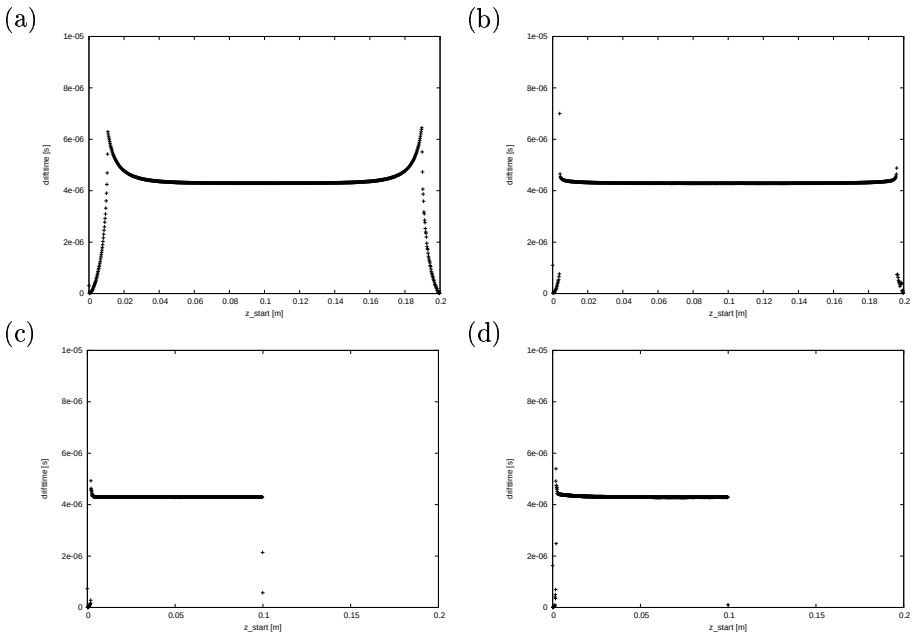

Figure 3.5: The drift time of e^- in the FEMLAB models as a function of the height z_{start} with (a) no rings, (b) 3 rings, (c) 6 rings, and (d) 9 rings to support the electric field at the end caps

	Radius	Potential
beam tube	9.525 mm	-50 V
cage wires	beam tube + 0.6 mm	-50 V
cathode wires	cage wires + 2 mm	0 V
anode	63.662 mm	500 V

Table 3.1: Parameters for the 2D GARFIELD field calculation.

3.3 Electron Drift in He/CO_2

As pointed out, for the reconstruction of ion tracks in the TACTIC drift region from the electron time-of-flight signals it is essential to know the relation between the drift time and their start position. This calibration was performed using GARFIELD[4] [26], a specialized drift chamber simulation software package. It uses MAGBOLTZ [27] to calculate the relevant electron transport properties of gas mixtures, taking into account electric and magnetic fields present.

The geometry used for this calculation is a 2D slice through the centre of the TACTIC cylinder ($x-y$ plane) including 32 pairs of cage and cathode wires with a diameter of 25 μm each. The gas mixture is 90/10 He/CO_2 at $p = 250$ mbar and $T = 293$ K. The other parameters are summarized in table 3.1 and the resulting electric field is shown in figure 3.6. Once the field is known, GARFIELD integrates the time an electron needs to travel from any point to the anode. The script employed is given in appedix B.3 and the results are shown in figure 3.7. As anticipated from the FEMLAB results (section 3.2.4), the drift time is of the order of μs. Obviously, the $r(t)$ relation is linear over a wide range far from the cathode wires. The field distortion caused by the wires affects the drift only in their proximity, causing inevitable uncertainties of the order of 0.1 mm in the radial position resolution.

[4] Version 7.10

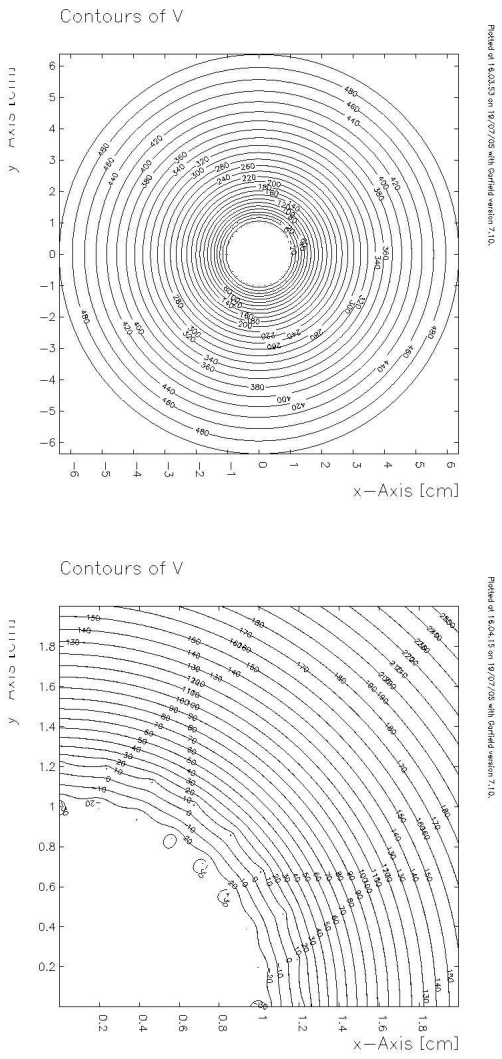

Figure 3.6: The electic field in the TACTIC drift region and its distortion near the cathode wires. Top — full view, bottom — magnified section. Note that the field becomes uniform in less than 1 cm from the cage and cathode wires.

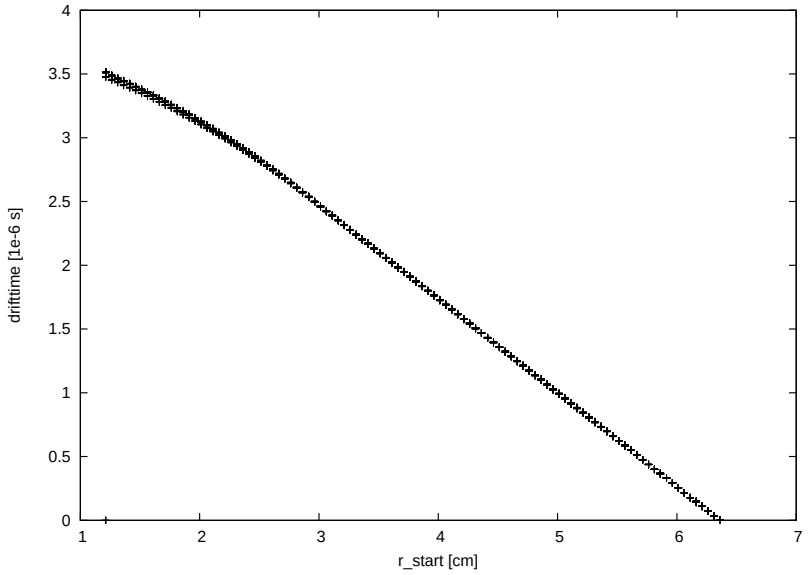

Figure 3.7: Arrival time of electrons (in μs) at the anode depending on their start radius. The spread of values is not due to statistics but to the field distortion in the proximity of the wires when going through different azimuthal start positions.

Chapter 4

Geant4 Simulation

4.1 What is Geant4?

For the simulation of the TACTIC chamber, a GEANT4 [28] framework is being used[1]. The purposes and capabilities of the GEANT4 package are outlined by its developers as follows [29]:

> GEANT4 is a toolkit for simulating the passage of particles through matter. It includes a complete range of functionality including tracking, geometry, physics models and hits. The physics processes offered cover a comprehensive range, including electromagnetic, hadronic and optical processes, a large set of long-lived particles, materials and elements, over a wide energy range starting, in some cases, from 250 eV and extending in others to the TeV range. ... [The toolkit] has been created exploiting software engineering and object-oriented technology and implemented in the C++ programming language. It has been used in applications in particle physics, nuclear physics, accelerator design, space engineering and medical physics.

However, the origins of GEANT4 are in the field of high energy physics, causing the support for low energy nuclear processes to be less comprehensive.

4.2 How Geant4 Works

GEANT4 provides the interfaces for three classes to be implemented by the user, specifying the detector geometry (`G4VUserDetectorConstruction`), the physics processes to be simulated (`G4VUserPhysicsList`), and the behaviour of the primary particle source (`G4VUserPrimaryParticleGenerator`). GEANT4 employs Monte Carlo methods to track particles through given geometries. All physics processes associated with a particle class suggest an interaction length or decay time. The process with the smallest step length is selected and the actions defined therein are carried out. Three different types of actions exist [29]:

[1] Version 6.0 Patch 01 as included in the SLAC distribution of March 2004.
See `http://geant4.slac.stanford.edu/g4cd/Welcome.html`

- *at rest*: what takes place even if the particle is not moving (e. g. radioactive decay)
- *along step*: what happens continuously (e. g. energy loss while moving)
- *post step*: what is done after the step (e. g. secondary particle production)

User-defined procedures can be added to the different layers of event and track processing performed:

- *Stepping*: represents every single-step taken
- *Tracking*: represents the information from a step needed to establish the particle track
- *Stacking*: priority handling for particle tracking
- *Event*: one single primary particle and whatever is triggered by it
- *Run*: a series of primary events

4.3 The TACTIC Chamber Simulation

4.3.1 Geometry and Materials

For the investigations carried out so far, a simplified model of the TACTIC detector has been implemented in a `G4VUserDetectorConstruction` subclass called `TacticDetectorConstruction` (TK[2]). It consists of a hollow tube representing the drift region that is filled with a 90% He/10% CO_2 gas mixture. On the outside there is a 3 mm copper layer making up the anode plane which was added to the simulation for the purpose of preventing particles from leaving the drift region and continuing to be tracked outside. Upstream and downstream sections of the beam tube, consisting of aluminum, are placed on the inside of the drift region.

The space between the two beam tube sections is vacuum within which a cylindrical volume containing the actual target gas (also 90/10 He/CO_2) is placed. Despite having physical inaccuracies, this configuration has been chosen in order to allow for flexible adjustments while investigating the ion kinematics and optimizing the chamber dimensions. Refer to figure 4.1 for an overview of the adjustable geometry parameters. The analysis of the ion energy loss per anode strip is facilitated by splitting up the drift region volume into a stack of identical cylindrical slices, each of which represents the "airspace" above one anode strip. This is because GEANT4 automatically ends a track and inserts a tracking point when a volume boundary is crossed.

4.3.2 Particles and Processes Involved

In `TacticPhysicsList` (GR[3]), subclass of `G4VUserPhysicsList`, the particles involved in the simulation are assigned the physics processes they are governed

[2]Initials in the text indicate the principal author of the classes.
[3]G. Ruprecht, TRIUMF

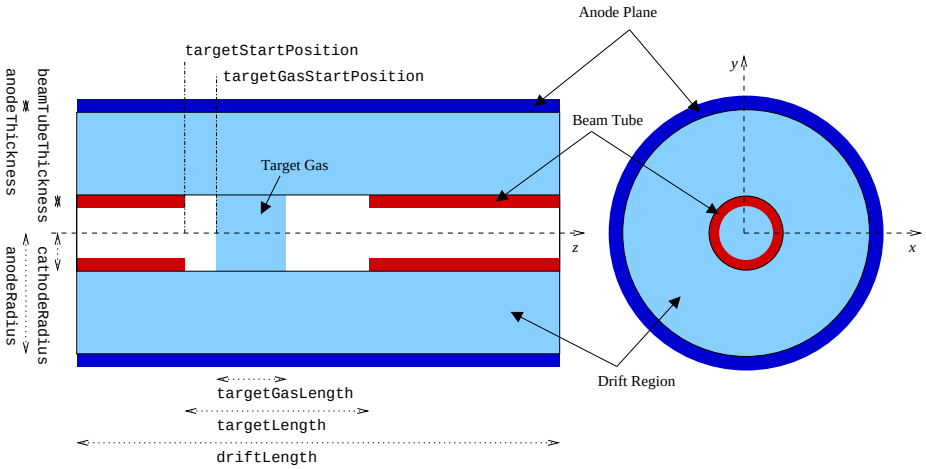

Figure 4.1: The GEANT4 detector geometry. Not shown is that the drift region in fact consists of `nAnodes` cylindrical slices. Note that the origin of the cartesian coordinate system is, by GEANT4 default, located in the centre of the geometry.

by. For the ^{8}Li(α,n)^{11}B reaction, only ions are considered, including α particles and protons. Electron movement is *not* simulated because of the unfeasibly huge requirements in computational power this would impose [30]. However, a table translating the location of δ-electron generation into the drift time can be computed externally (see section 3.3) and included into the simulation. All the physics processes described in this section are taken into account.

Stopping Power

When ions travel through matter, their energy decreases, primarily due to ionization. The stopping power is described by the Bethe-Bloch formula [31]:

$$\frac{\mathrm{d}E}{\mathrm{d}x} = -N_{\mathrm{el}}\frac{Z_{\mathrm{h}}^2}{\beta^2}\left[\ln\left(\frac{2m_e\beta^2\gamma^2 T_{\max}}{I^2}\right) - 2\beta^2 - \delta - 2\frac{C_e}{Z}\right] \tag{4.1}$$

where

$$\begin{aligned}
N_{\mathrm{el}} &= \text{electron density of the medium}\\
Z_{\mathrm{h}} &= \text{charge of the ion}\\
m_e &= \text{mass of an electron}\\
\beta &= \frac{v}{c} \text{ with } v: \text{ ion velocity, } c: \text{ speed of light}\\
\gamma &= \frac{1}{\sqrt{1-\beta^2}}\\
I &= \text{average ionisation potential}\\
Z &= \text{atomic number}\\
\delta, \frac{C_e}{Z} &= \text{correction terms } (\textit{density correction}, \textit{shell correction})\\
T_{\max} &= \text{maximum energy transfer from ion to free electron}
\end{aligned}$$

and

$$T_{\max} = \frac{2m_e\left(\gamma^2 - 1\right)}{1 + 2\gamma\frac{m_e}{M} + \left(\frac{m_e}{M}\right)^2}$$

where M denotes the ion mass.

For $\beta < 0.05$, corresponding to 1.2 MeV/u, (4.1) becomes inaccurate [31]. Extensions for lower energies are available in `G4hLowEnergyIonisation` [31, 32, 33]. For $\beta < 0.01$, it is assumed that the stopping power is proportional to v, whereas for $0.01 < \beta < 0.05$ this object relies entirely on parameterizations of experimental data, supplied in various tables [31].

Multiple Scattering

`G4MultipleScattering` takes care of the elastic scattering of charged particles in a medium. A thorough description can be found in ref. [33].

Nuclear Reaction

The `LENuclearReactionProcess` (GR) representing a low energy nuclear reaction was implemented in a generic, TACTIC-independent way, although it was tailored to ^{8}Li(α,n)^{11}B. The cross section for ^{8}Li+α is set to some base value (3×10^{10} mb), but it is zero for projectiles that have already lost more than 10% of the beam energy, as well as for any other reaction. If a "reaction" occurs, an ejectile is created and its ejection angle and energy are calculated using (1.17) and (1.18), respectively. However, the projectile is intentionally *not* destroyed by the reaction, but continues its way through the detector geometry, allowing for a large number of interactions. Moreover, other exit channel particles (n in the case of ^{8}Li(α,n)^{11}B) are ignored.

4.3.3 Generation of Primary Particles

Primary particles are created in `TacticPrimaryGenerator`, implementing the `G4VUserPrimaryParticleGeneratorAction` interface. Actually, two different implementations of this object have been realized. On the one hand, it can be operated as a representation of the incoming ion beam, simply emitting a projectile ion, defined by its atomic and mass numbers and excitation energy, along the z axis at a given beam energy (GR). On the other hand, by switching code, it can act as the emitter of ^{11}B ejectiles at a given c.m. angle (TK). In this case, the laboratory frame angle and the ejectile energy are calculated in the same way as with the `LENuclearReactionProcess`, taking into account a given projectile energy so that the simulated reaction can be confined to a well-known position.

4.3.4 Ion Tracking

`TacticRunEventAction` (GR, TK), a subclass of both `G4UserRunAction` and `G4UserEventAction`, defines actions carried out before and after a run (involving a certain number of primaries) and after each single event. This comprises the output of the ion track point coordinates as well as the mean radii that would be detected by the anode rings after calibration. The latter are

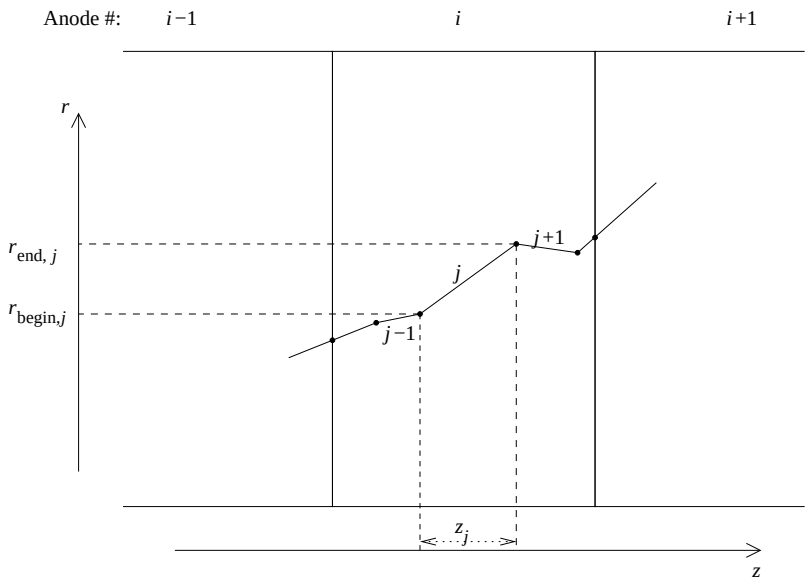

Figure 4.2: Algorithm for simulated r signals. The dots represent track points. The segmentation of the drift region volume (see section 4.3.1) generates a new track point when the area of a new anode ring is entered. Refer to text for further explanation.

calculated from the track points in `TacticSteppingAction` (TK), subclass of `G4UserSteppingAction`. Since more than one track may begin and end within reach of the i-th anode ring, they are weighted by their z projection z_j (see figure 4.2):

$$r_i = \frac{\sum_j 0.5\,(r_{\mathrm{begin},j} + r_{\mathrm{end},j})\,z_j}{\sum_j z_j}$$

where

$$z_j = \left|(\vec{r}_{\mathrm{end},j})_z - (\vec{r}_{\mathrm{begin},j})_z\right|$$

At the same time, the energy loss occurring over each anode ring is obtained through `G4hLowEnergyIonisation`. Rather than using an energy cut for δ-electron production, they are always created by the `G4hLowEnergyIonisation` process. In order to prevent them from being tracked, they are destroyed in `TacticStackingAction` (TK), subclass of `G4UserStackingAction`, immediately after being counted.

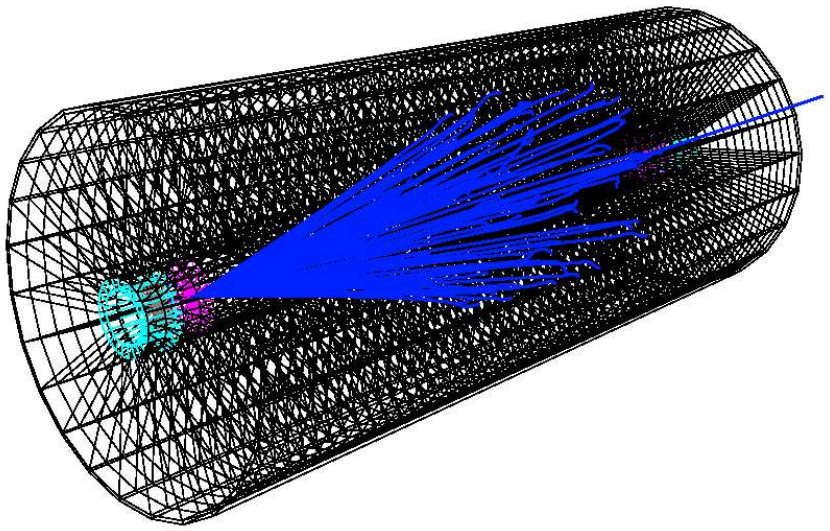

Figure 4.3: A series of ion tracks (blue) caused by an incident beam of ^{8}Li at 9 MeV

4.4 Application

4.4.1 Chamber Dimensions

For an active length of the detector for ^{8}Li(α,n)^{11}B of 240 mm, it was found that a GEM radius of 60 mm would be desirable[4]. This configuration, when operated at 250 mbar and with a maximum beam energy of 9 MeV, allows all ejectiles to stop within the drift region, with only a few statistical exceptions [11].

4.4.2 Vertex and Angle Reconstruction

It is essential to reliably reconstruct the location of the nuclear reaction within the target gas, for the projectile energy depends sensitively on the target penetration depth. Also, from the observed mean radial distances from the anode strips, the c.m. angle of a reaction event should be inferable. The simulation program described in section 4.3 has been used to generate data so that the achievable resolution in vertex point and c.m. angle can be studied. The set of parameters (see section 4.3.1) employed is summarized in table 4.1. `TacticPrimaryGenerator` was operated in the "eject ^{11}B at given location" mode. For all c.m. angles $0° \leq \vartheta^{\text{c.m.}} \leq 180°$, in steps of 1°, 10000 events were generated at the position ($x = 0$, $y = 0$, $z = -100$ mm), i. e. at the edge of

[4]GEMs are available at a size of 240 × 200 mm. Using one of them for each half cylinder, the GEM radius will in fact be about 200 mm/π = 63.7 mm

`anodeRadius`	50 mm
`cathodeRadius`	10 mm
`driftLength`	240 mm
`targetLength`	220 mm
`targetGasLength`	200 mm
`nAnodes`	48
`beamTubeThickness`	3 mm
`anodeThickness`	1 mm
Target gas = drift gas	90% He, 10% CO_2
Pressure	250 mbar
Temperature	293 K (room temp.)

Table 4.1: The parameters for the GEANT4 simulation. The target region and target gas region are centered around $z = 0$.

the target gas. The mean radii r_i as detected by the anode rings after TOF calibration (whose uncertainties were not taken into account) were subjected to a simple least-squares fit [34] yielding a regression line

$$r(i) = a \times i + b \tag{4.2}$$

where $0 \leq i \leq 47$. Then the vertex point and the lab angle are given by

$$z_{\text{vertex}} = \left(-\frac{b}{a} + \frac{1}{2}\right) l_{\text{Anode}} - \frac{1}{2} l_{\text{Drift}} \tag{4.3}$$

and

$$\vartheta = \arctan \frac{a}{l_{\text{Anode}}} \tag{4.4}$$

where l_{Anode} is the width of one anode ring, and $l_{\text{Drift}} \equiv$ `driftLength`. The C++ code accomplishing this task is given in appendix C.2. Keeping in mind that the coordinate origin is situated at the centre of the detector, one half of the chamber length is subtracted in (4.3). The beam straggling is small enough to justify the assumption that the reaction takes place on the z axis.

Weighted by the number of anodes by which an event is detected, where a minimum of two anodes is required, z_{vertex} and ϑ were averaged. The average of the corresponding square deviations serves as a measure of accuracy.

The results can be seen in figures 4.4 and 4.5. It is obvious that the vertex point can be reconstructed moderately well only in a range of about $60° \leq \vartheta^{\text{c.m.}} \leq 120°$. Surprisingly, this does not coincide with the maximum of the anodes detecting the event. Moreover there seems to be a systematic error of about 1 mm. The best accuracy obtainable is about $\Delta z_{\text{vertex}} = 5$ mm (5 %). Note that the statistics of 10000 simulated events will not be available in the real experiment.

The $\vartheta^{\text{c.m.}}$ reconstruction is accomplished by using the slope of the regression line (4.2). Since the accuracy is apparently better than with the vertex reconstruction, the high uncertainties in the latter seem to be caused primarily by the ordinate axis intercept. The range of smallest uncertainties in $\vartheta^{\text{c.m.}}$ does coincide with the maximum of affected anodes. It is apparent that no reasonable

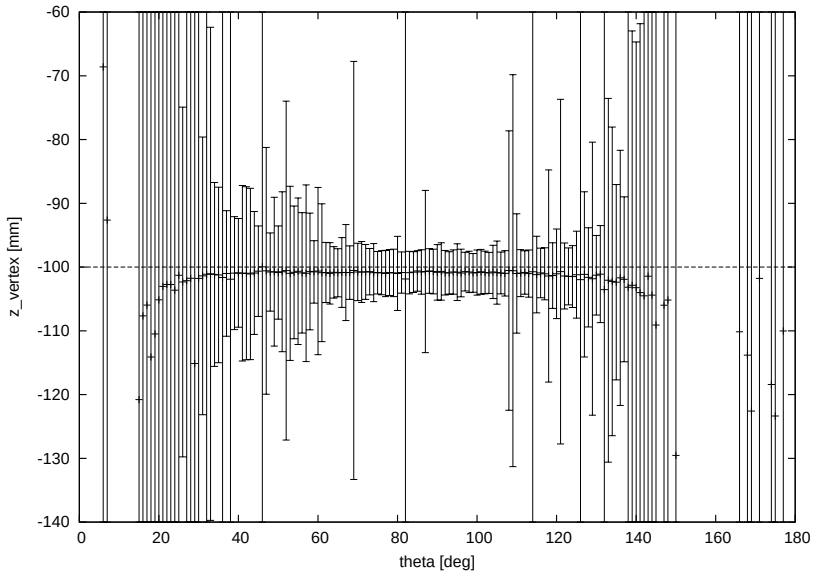

Figure 4.4: Accuracy of vertex point reconstruction. See text for details.

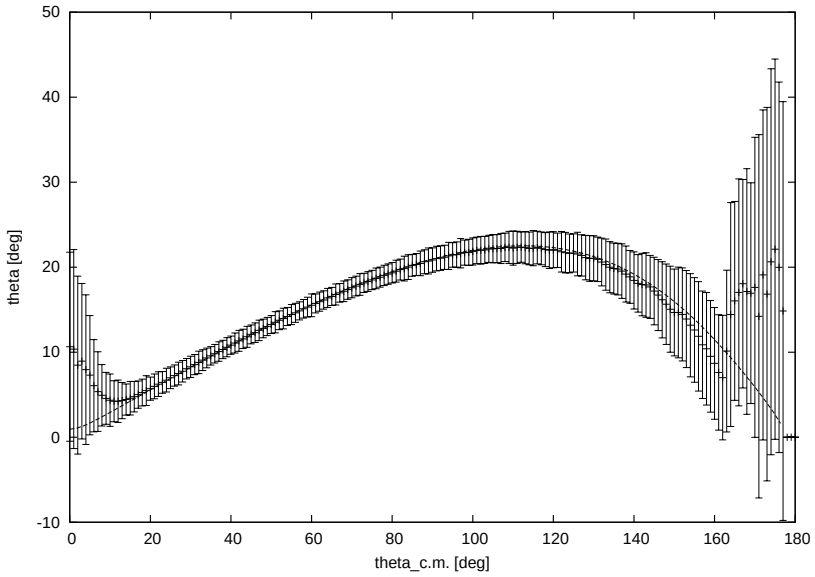

Figure 4.5: Accuracy of lab angle reconstruction. The dashed theory curve is given by (1.17) and (1.18). See text for details.

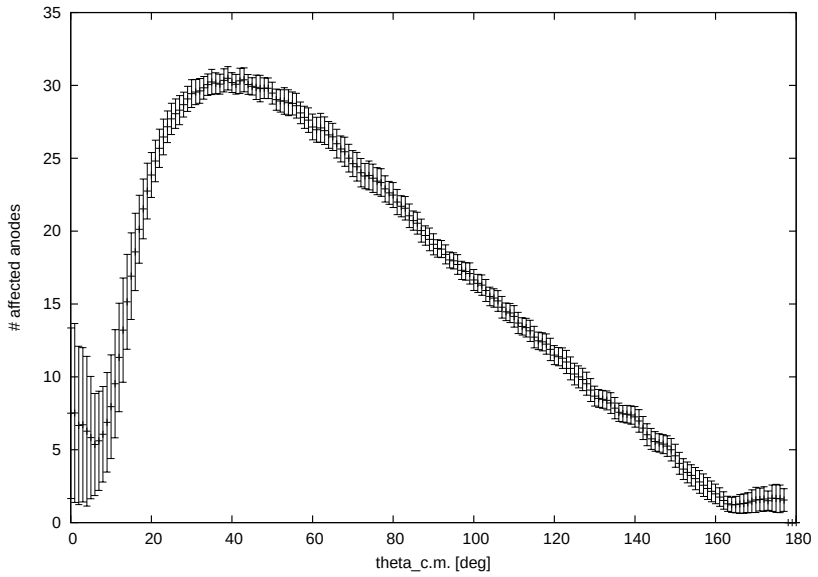

Figure 4.6: The number of anodes detecting an event. The errorbars indicate the standard deviation.

conclusions can be drawn when the ejectile trajectory passes less than five anode rings. However, note that, according to the simulation results, an observed lab angle of, say, 20° may correspond to any $\vartheta^{\text{c.m.}}$ between 75° and 145°!

4.5 Outlook

The above results give rise to suspecting the `G4MultipleScatteringProcess` to yield unrealistic results, causing the ion straggling to be too high. Comparisons with SRIM [35] simulation data, showing some differences in the results for heavy ion ranges, suggest the same. Future work may need to be devoted to investigating this behaviour. More sophisticated analysis is required to extrapolate the ion track to its starting point, reducing the high uncertainty and eliminating the apparent systematic error.

Advancing the TACTIC simulation program involves adding the ^{8}Li elastic scattering process, which is going to be the main source of background, and the ^{8}Li decay process (^{11}B is stable). The $r(t)$ relation should be included in the simulation once it is established externally for the actual chamber layout (see section 3.3). Also, Monte Carlo methods could be used to derive the final anode signal shapes by taking into account their directional straggling. Eventually, the γ-rays emitted in the reaction should be included in the simulation. Their detection takes place outside the TACTIC chamber and its enclosure, resulting in an energy attenuation. To accomodate this, the complete mechanical layout must be entered into the simulation environment.

Chapter 5

Conclusions

At the time of writing, the mechanical layout of the TACTIC detector had not yet been finalized. Naturally, many technical specifications are subject to change throughout the development process. As a result, the work presented in this report relies on varying dimensions, applied voltages etc. However, in most cases adjustments can easily be done once all parameters are known, quickly modifying source code to generate more realistic results.

The test chamber data acquisition upgrade will be useful for future measurements while the flash-ADCs are not yet operational. The relative signal gain measured complements previous observations.

By calculating the electric field in the drift region, the required effect of the design option involving biased ring pads was confirmed. A calibration curve was calculated, enabling ion tracking by linking time-of-flight signals to track points

After further development, the GEANT4 simulation will be instrumental in providing the possibility of comparing future experimental data with it. Moreover, new GEANT4 components developed might be shared with the worldwide user community, extending the usability range of the simulation package.

To sum up, progress was achieved in helping make the TACTIC detector a powerful new tool in experimental nuclear astrophysics.

Appendix A

Test Chamber Measurements

A.1 Test Chamber Runs and Gain Factors

The duration of the data taking runs listed below was about two minutes each. The α source was 45 mm distant from the anode strip used. See appendix A.2 for the spectra obtained.

Run No.	Pressure [mbar]	$V_{\mathrm{GEM+anode}}$ [V]	Event Rate [1/s]	s_V	$s_V s_p$	Gain
282	500	1000	245	1.64	0.7052	1.42
283	500	1050	738	1.54	0.6622	1.51
284	500	1100	1200	1.44	0.6192	1.61
285	500	1150	1370	1.21	0.5203	1.92
287	500	1200	1409	1	0.43	2.33
288	600	1000	277	1.69	0.8957	1.12
289	600	1050	874	1.62	0.8586	1.16
290	600	1100	1273	1.44	0.7632	1.31
291	600	1150	1355	1.22	0.6466	1.55
292	600	1200	1399	1	0.53	1.89
293	600	1250	1429	0.79	0.4187	2.39
294	600	1300	1460	0.6	0.318	3.14

Table A.1: Overview of the TACTIC test chamber runs, the spectra scaling factors and the resulting gain (1/2).

Run No.	Pressure [mbar]	Voltage [V]	Event Rate [1/s]	s_V	$s_V s_p$	Gain
235	700	1000	595	1.89	1.2096	0.83
236	700	1050	1106	1.74	1.1136	0.9
237	700	1100	1217	1.51	0.9664	1.03
238	700	1150	1315	1.24	0.7936	1.26
239	700	1200	1334	1	0.64	1.56
240	700	1250	1333	0.79	0.5056	1.98
241	700	1300	1277	0.62	0.3968	2.52
242	700	1350	1484	0.48	0.3072	3.26
243	700	1400	1560	0.37	0.2368	4.22
245	800	1000	595	2.01	1.5075	0.66
246	800	1050	998	1.8	1.35	0.74
247	800	1100	1165	1.5	1.125	0.89
248	800	1150	1245	1.24	0.93	1.08
249	800	1200	1285	1	0.75	1.33
250	800	1250	1250	0.78	0.585	1.71
251	800	1300	1385	0.61	0.4575	2.19
252	800	1350	1362	0.48	0.36	2.78
253	800	1400	1511	0.35	0.2625	3.81
254	800	1450	1528	0.27	0.2025	4.94
255	900	1000	597	2.19	1.9272	0.52
256	900	1050	911	1.84	1.6192	0.62
257	900	1100	1094	1.61	1.4168	0.71
258	900	1150	1152	1.3	1.144	0.87
259	900	1200	1210	1	0.88	1.14
260	900	1250	1211	0.77	0.6776	1.48
261	900	1300	1268	0.58	0.5104	1.96
262	900	1350	1448	0.44	0.3872	2.58
263	900	1400	1460	0.34	0.2992	3.34
264	900	1450	1522	0.25	0.22	4.55
265	900	1500	1628	0.19	0.1672	5.98
267	1000	1000	365	1.99	1.99	0.5
268	1000	1050	684	1.84	1.84	0.54
269	1000	1100	899	1.64	1.64	0.61
270	1000	1150	1023	1.27	1.27	0.79
273	1000	1200	1098	1	1	1
274	1000	1250	1140	0.74	0.74	1.35
275	1000	1300	1178	0.55	0.55	1.82
276	1000	1350	1306	0.41	0.41	2.44
278	1000	1400	1352	0.3	0.3	3.33
279	1000	1450	1469	0.22	0.22	4.55
280	1000	1500	1485	0.17	0.17	5.88

Table A.2: Overview of the TACTIC test chamber runs, the spectra scaling factors and the resulting gain (2/2).

A.2 Test Chamber ADC Spectra

The ADC spectra from one channel of the TACTIC test chamber for the runs listed in appendix A.1 are given below. They show the number of counts for each ADC value bin.

A.2.1 $p = 500$ mbar

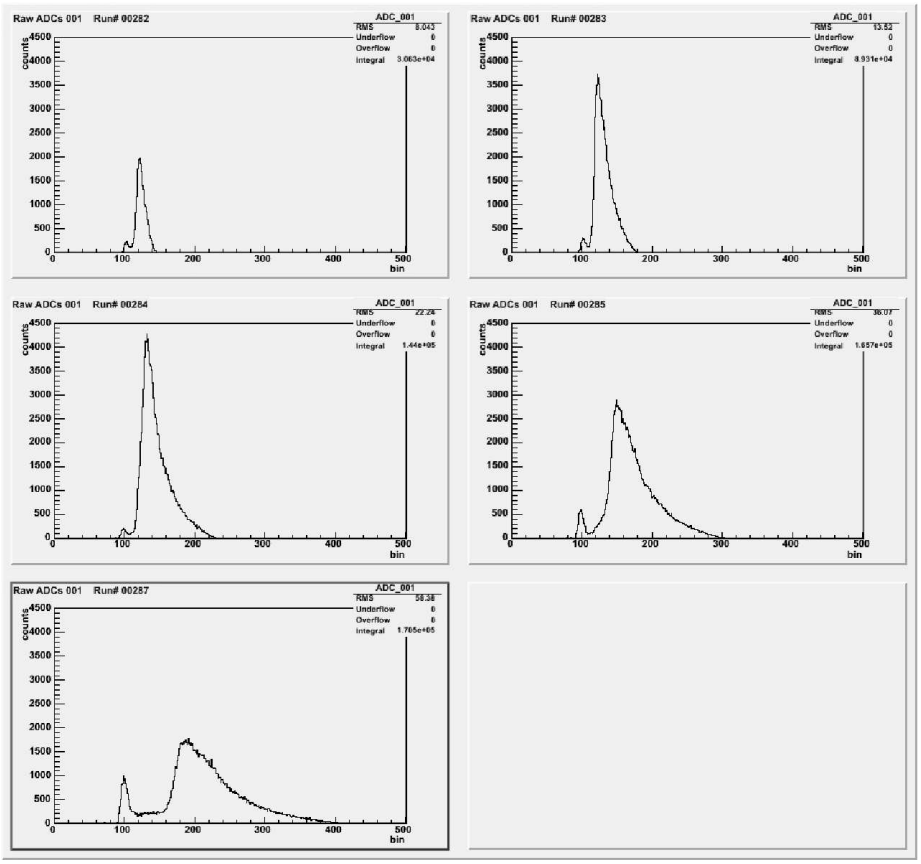

Figure A.1: ADC spectra at $p = 500$ mbar.

A.2.2 $p = 600$ mbar

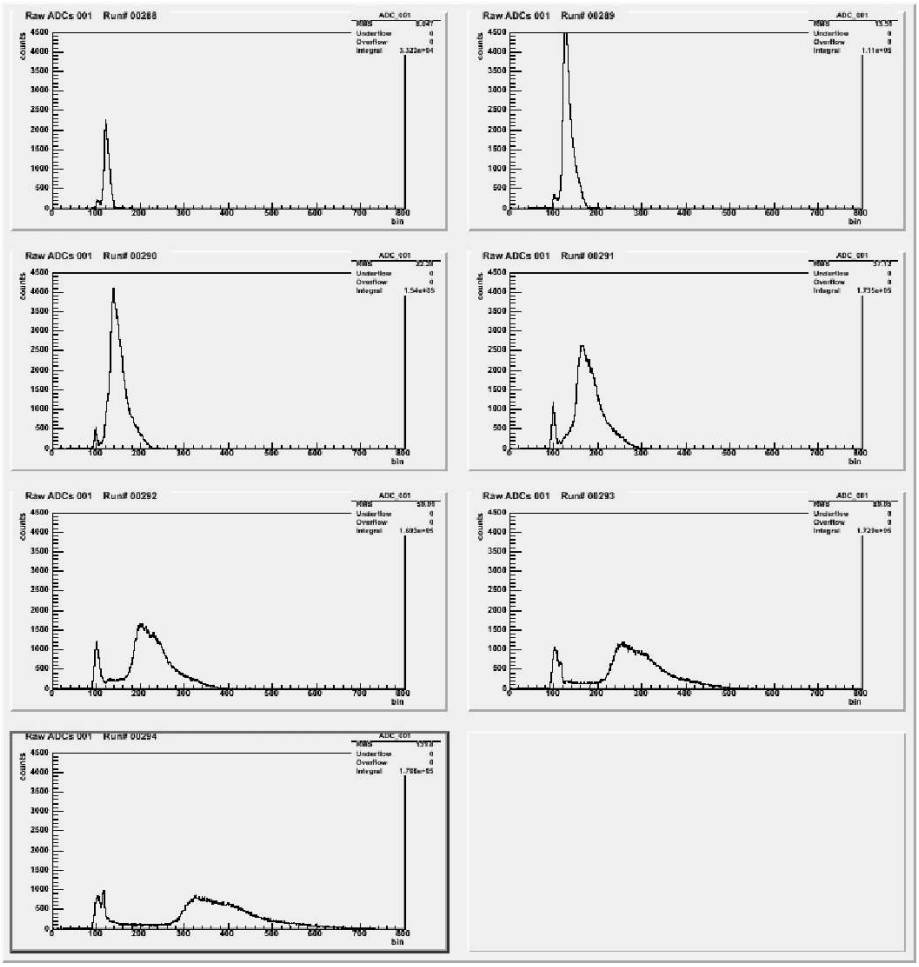

Figure A.2: ADC spectra at $p = 600$ mbar.

A.2.3 $p = 700$ mbar

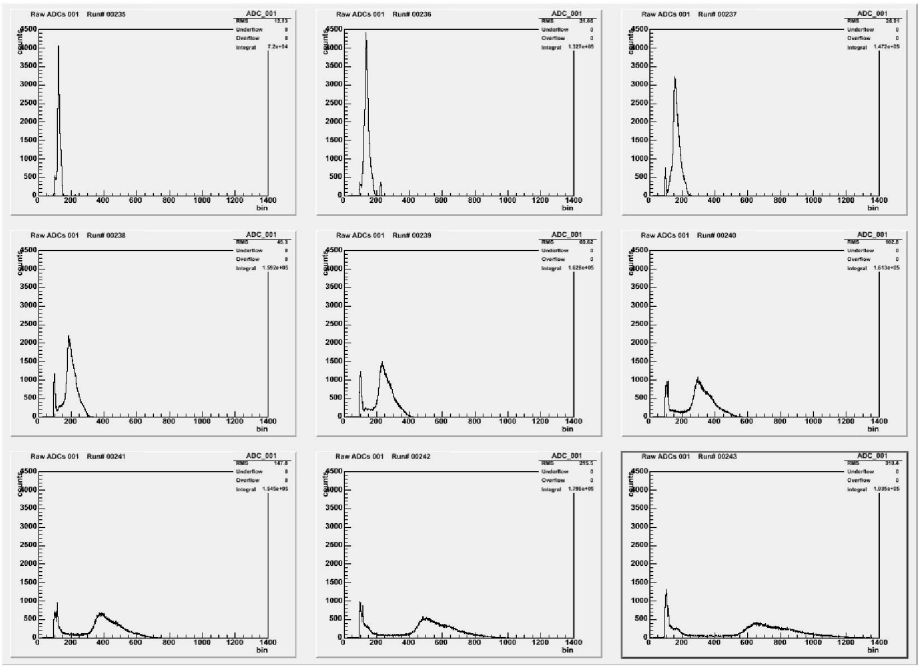

Figure A.3: ADC spectra at $p = 700$ mbar. In run 236, a small peak around channel 225 is due to a laser device temporarily operated in the proximity of the setup.

A.2.4 $p = 800$ mbar

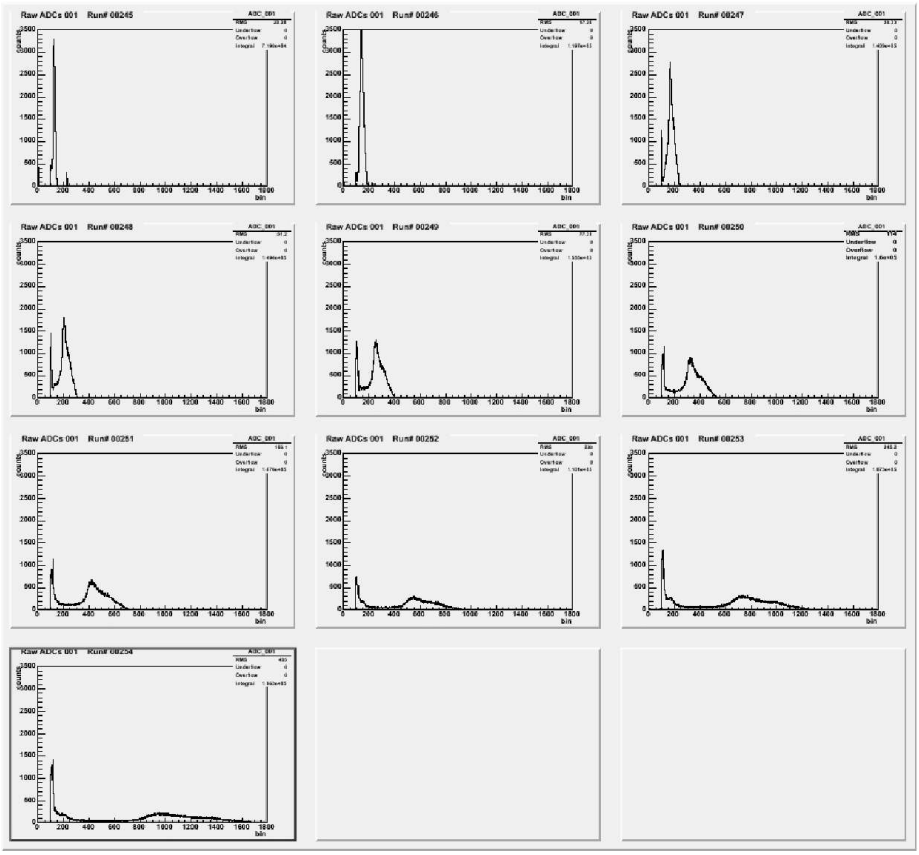

Figure A.4: ADC spectra at $p = 800$ mbar.

A.2.5 $p = 900$ mbar

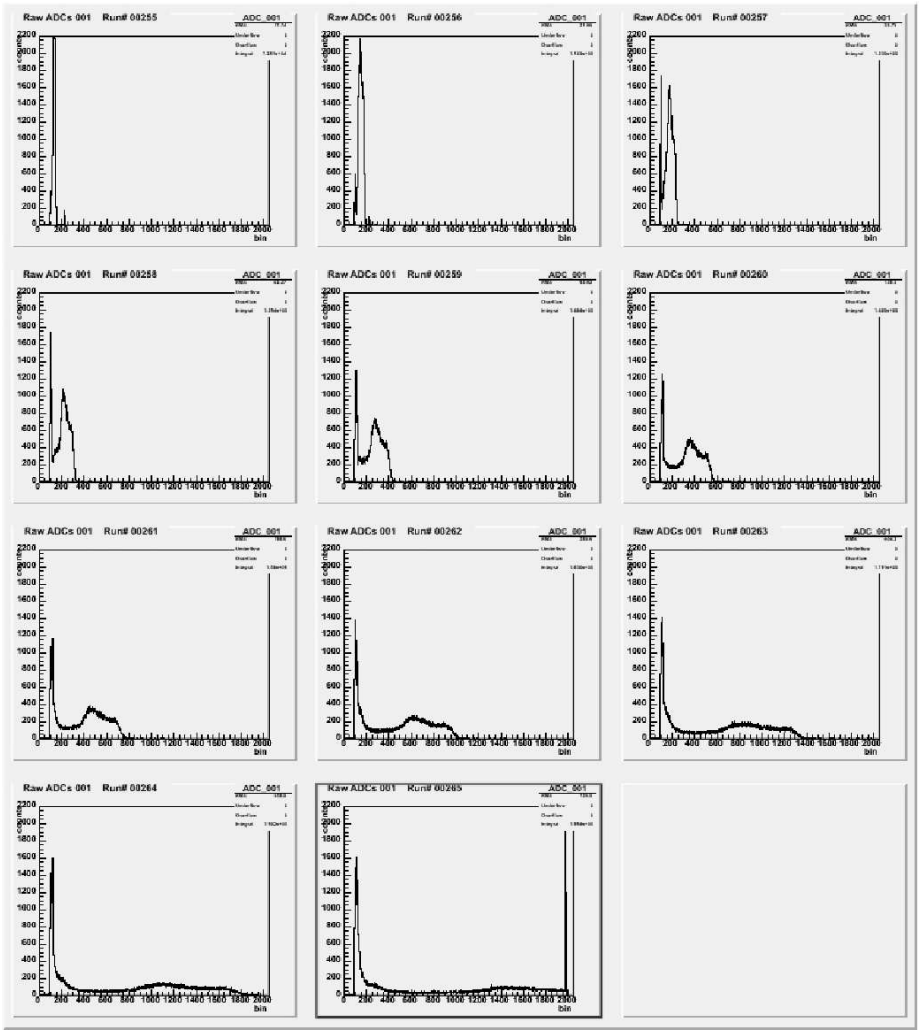

Figure A.5: ADC spectra at $p = 900$ mbar.

A.2.6 $p = 1000$ mbar

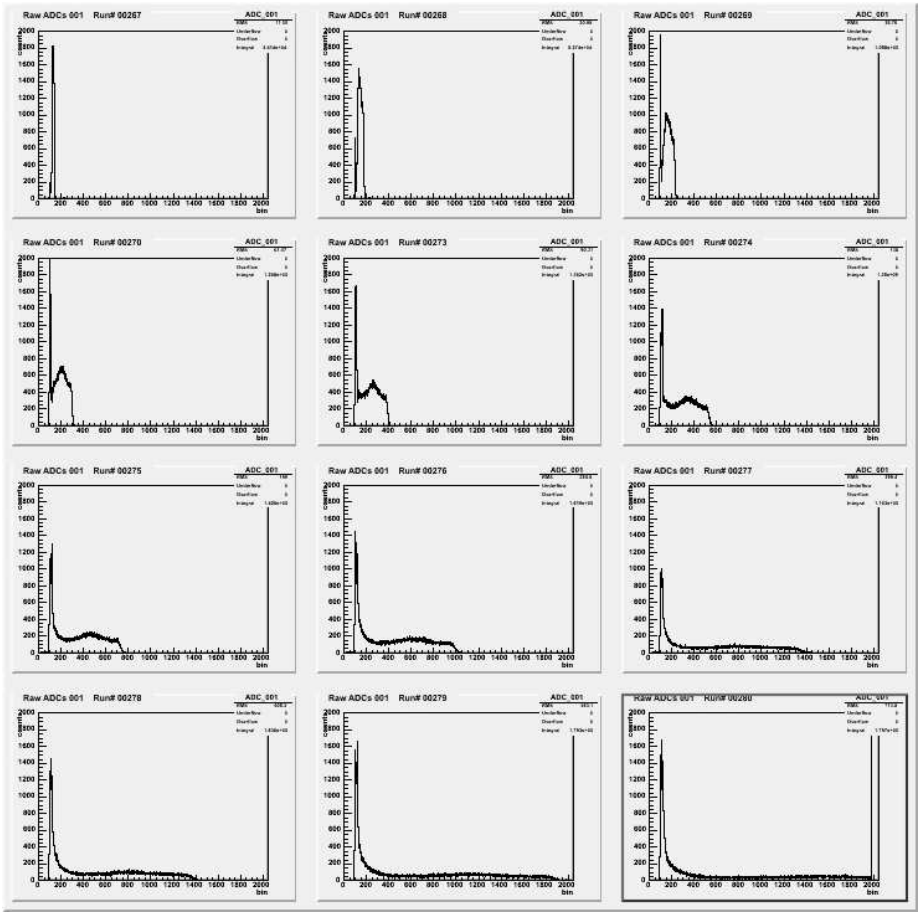

Figure A.6: ADC spectra at $p = 1000$ mbar.

Appendix B

Drift Field Analysis

B.1 Femlab Models

The FEMLAB models used as described in section 3.2. d is the thickness of the ring pads.

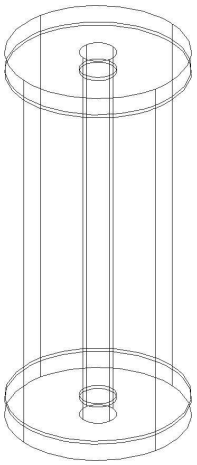

Figure B.1: FEMLAB model geometry (no rings)

← *No rings*

3 rings →

r = 21-24 mm: U_1 = -248.1 V
r = 29-32 mm: U_2 = -153.6 V
r = 37-40 mm: U_3 = -81.2 V

$d = 200\ \mu$m

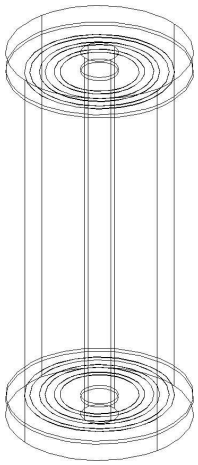

Figure B.2: FEMLAB model geometry (3 rings)

6 rings

r = 13-16 mm: U_1 = -384.6 V
r = 19-22 mm: U_2 = -277.0 V
r = 25-28 mm: U_3 = -197.2 V
r = 31-34 mm: U_4 = -133.8 V
r = 37-40 mm: U_5 = -81.2 V
r = 43-46 mm: U_6 = -36.2 V

$d = 100\ \mu$m

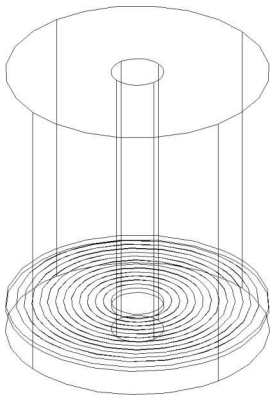

Figure B.3: FEMLAB model geometry (6 rings)

9 rings

r = 13-14 mm: U_1 = -406.8 V
r = 17-18 mm: U_2 = -326.1 V
r = 21-22 mm: U_3 = -262.2 V
r = 25-26 mm: U_4 = -209.2 V
r = 29-30 mm: U_5 = -163.9 V
r = 33-34 mm: U_6 = -124.4 V
r = 37-38 mm: U_7 = -89.4 V
r = 41-42 mm: U_8 = -57.9 V
r = 45-46 mm: U_9 = -29.3 V

$d = 100\ \mu$m

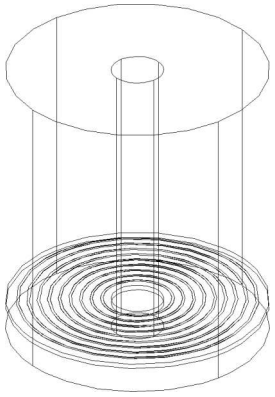

Figure B.4: FEMLAB model geometry (9 rings)

B.2 Analysis of Femlab Field Data

The following code implements the algorithm described in section 3.2.3. The FEMLAB output files were pre-edited to contain the x coordinates of all grid points in the first line and the z coordinates in the second line. This was saved to `coordfile.txt`. In `xfile.txt` and `zfile.txt`, the coordinate lines were deleted, leaving only the matrix of E_x and E_z values, respectively, at the grid points. FEMLAB writes `NaN` (*Not a Number*) if a grid point is outside the geometry. To facilitate the read-in in C++, the `NaN`s were replaced by 0 (which does not affect the analysis since only grid points within the geometry are considered). The parameter `zrange` in line 10 of the code is to be set to 0.2 in the case of the models with no and 3 rings, and to 0.1 for the 6- and 9-ringed models.

```
0000:  #include <iostream.h>
0001:  #include <fstream.h>
0002:  #include <math.h>
0003:  #include <stdio.h>

0004:  /********* global variables *******************************/
0005:  double R1;
0006:  double R2;
0007:  const long numberOfGridpointsX = 1000;
0008:  const long numberOfGridpointsZ = 1000;
0009:  const double xrange = 0.04;  // in m
0010:  const double zrange = 0.1;   // in m

0011:  const double xstep = 0.1 / numberOfGridpointsX;
0012:  const double zstep = zrange / numberOfGridpointsZ;

0013:  double x[numberOfGridpointsX];
0014:  double z[numberOfGridpointsZ];
0015:  double Ex[numberOfGridpointsX][numberOfGridpointsZ];
0016:  double Ez[numberOfGridpointsX][numberOfGridpointsZ];

0017:  /******** technical stuff *********************************/
0018:  int signum(double d) {
0019:    if (d < 0) {
0020:      return -1;
0021:    } else {
0022:      return 1;
0023:    }
0024:  }

0025:  double distance(double x1, double x2, double z1, double z2) {
0026:    double deltax = fabs(x2-x1);
0027:    double deltaz = fabs(z2-z1);
0028:    return sqrt(deltax*deltax + deltaz*deltaz);
0029:  }

0030:  /* returns the array index of the grid point closest to a given point
0031:   * in x direction */
0032:  long findClosest_i(double x0, double z0) {
0033:    long closestIndex = 0;
0034:    double closestDistance = distance(x0, x[closestIndex], z0, z0);
0035:    double dist;
0036:    for (long i=0; i<numberOfGridpointsX; i++) {
0037:      dist = distance(x0, x[i], z0, z0);
0038:      if ( (dist < closestDistance) && (fabs(x[i]) >= R1) ) {
0039:        closestDistance = dist;
0040:        closestIndex = i;
0041:      }
0042:    }
0043:    return closestIndex;
0044:  }

0045:  /* returns the array index of the grid point closest to a given point
0046:   * in z direction */
0047:  long findClosest_k(double x0, double z0) {
0048:    long closestIndex = 0;
0049:    double closestDistance = distance(x0, x0, z0, closestIndex*zstep);
```

```
0050:    double dist;
0051:    for (long k=0; k<numberOfGridpointsZ; k++) {
0052:      dist = distance(x0, x0, z0, z[k]);
0053:      if (dist < closestDistance) {
0054:        closestDistance = dist;
0055:        closestIndex = k;
0056:      }
0057:    }
0058:    return closestIndex;
0059:  }

0060:  // returns the index of the smallest value in an array
0061:  long getMinIndex(double a[], long i1, long i2) {
0062:    double minValue = a[i1];
0063:    long minIndex = i1;
0064:    for (long i=i1; i<i2; i++)
0065:      if (a[i] < minValue) {
0066:        minIndex = i;
0067:        minValue = a[i];
0068:      }
0069:    return minIndex;
0070:  }

0071:  /********* physics ******************************/

0072:  /* returns the drift velocity of an electron depending
0073:   * on the local electric field */
0074:  double driftvelocity(double E) {
0075:    return 0.9 * fabs(E);
0076:  }

0077:  /********** MAIN ******************************/
0078:  int main(int argc, char **argv) {

0079:    char xfilestr[256]      = "";
0080:    char zfilestr[256]      = "";
0081:    char coordfilestr[256]  = "";
0082:    char configfilestr[256] = "";
0083:    char outfilestr[256]    = "";
0084:    strcat(xfilestr, argv[1]);
0085:    strcat(zfilestr, argv[1]);
0086:    strcat(coordfilestr, argv[1]);
0087:    strcat(configfilestr, argv[1]);
0088:    strcat(outfilestr, argv[1]);

0089:    /* read radii of chamber */
0090:    ifstream configfile(strcat(configfilestr, "/configfile.txt"));
0091:    configfile >> R1;
0092:    configfile >> R2;
0093:    configfile.close();

0094:    /* read coordinates from FEMLAB output text file */
0095:    ifstream coordfile(strcat(coordfilestr,"/coordfile.txt"));
0096:    double xnow;
0097:    for (long i=0; i<numberOfGridpointsX; i++) coordfile >> x[i];
0098:    for (long k=0; k<numberOfGridpointsZ; k++) coordfile >> z[k];
0099:    coordfile.close();

0100:    /* read electric field data from FEMLAB output text file */
0101:    ifstream xfile(strcat(xfilestr,"/xfile.txt"));
0102:    ifstream zfile(strcat(zfilestr,"/zfile.txt"));
0103:    for (long k=0; k<numberOfGridpointsZ; k++) {
0104:      for (long i=0; i < numberOfGridpointsX; i++) {
0105:        xfile >> Ex[i][k];
0106:        zfile >> Ez[i][k];
0107:      }
0108:    }
0109:    xfile.close();
0110:    zfile.close();

0111:    /*----------------------------------------*/
0112:    /* loop through all start points of electric field lines */
0113:    ofstream outfile(strcat(outfilestr,"/field.dat"));
```

```
0114:    long loopcount = 0;
0115:    const long MAXLOOPCOUNT = numberOfGridpointsX;

0116:    long outIndex = 0;
0117:    double loopstep = zstep;
0118:    const long numberOfLoopRuns = (long) (zrange / loopstep);

0119:    double z_start_a[numberOfLoopRuns];
0120:    double delta_z_a[numberOfLoopRuns];
0121:    double drifttime_a[numberOfLoopRuns];

0122:    for (double z_start=0; z_start<=zrange; z_start+=loopstep) {
0123:      double drifttime = 0;
0124:      double x_start = R1;
0125:      double delta_z = 0;
0126:      double delta_z_new;
0127:      double delta_znew;

0128:      long i = findClosest_i(x_start, z_start);
0129:      long k;

0130:      double Ex_local;
0131:      double Ez_local;

0132:      double xnew = x[i];
0133:      double znew = z_start;

0134:      while ( (xnew <= R2) && (xnew >= R1) && (znew >= 0) && (znew <= zrange)) {
0135:        k = findClosest_k( xnew, znew );
0136:        i = findClosest_i( xnew, znew );

0137:        Ex_local = Ex[i][k];
0138:        Ez_local = Ez[i][k];

0139:        xnew += -signum(Ex_local) * xstep;
0140:        delta_znew = ( Ez_local / Ex_local ) * xstep;
0141:        znew += delta_znew;

0142:        if ((znew < 0) || (znew > zrange)) break;

0143:        drifttime += sqrt(xstep*xstep + delta_znew*delta_znew) /
                driftvelocity(sqrt(Ex_local*Ex_local + Ez_local*Ez_local));

0144:        delta_z_new = fabs(znew - z_start);
0145:        if (delta_z_new > delta_z) {
0146:           delta_z = delta_z_new;
0147:           loopcount = 0;
0148:        }

0149:        // Emergency Break to avoid infinite loops
0150:        loopcount++;
0151:        if (loopcount > MAXLOOPCOUNT) {
0152:           cout << z_start << ": MAXLOOPCOUNT" << endl;
0153:           break;
0154:        }
0155:      }

0156:      outfile << z_start << " " << delta_z << " " << drifttime << endl;

0157:      z_start_a[outIndex] = z_start;
0158:      delta_z_a[outIndex] = delta_z;
0159:      drifttime_a[outIndex] = drifttime;

0160:      outIndex++;
0161:    }
0162:    outfile.close();

0163:    return 0;
0164:  }
```

B.3 Electron Arrival Times in Garfield

The below GARFIELD script writes the time an electron needs to travel from the point given by r and φ to the anode to file.

```
0000:  !add postscript type ps_portrait file-name tactic.ps
0001:  !open postscript
0002:  !activate postscript
0003:  // --- quantities stated in cm ---
0004:  // outer radius of beam tube
0005:  GLOBAL beamTubeR = 0.9525

0006:  // radius at which cage wires are mounted
0007:  GLOBAL cageR     = beamTubeR + 0.06

0008:  // radius at which anodes are situated
0009:  GLOBAL anodeR    = 6.3662

0010:  // radius at which cathode wires are mounted
0011:  GLOBAL cathodeR  = cageR + 0.2

0012:  // diameter of a wire
0013:  GLOBAL wireD     = 0.0025    // 25 um

0014:  // --- quantities stated in V ---
0015:  // cathode voltage
0016:  GLOBAL cathodeV  = 0

0017:  // voltage of cage wires
0018:  GLOBAL cageV     = cathodeV - 50

0019:  // voltage of beam tube
0020:  GLOBAL beamTubeV = cageV

0021:  // voltage of anodes
0022:  GLOBAL anodeV    = 500

0023:  // --- wire specs ---
0024:  // number of cage wires == number of cathode wires
0025:  GLOBAL nWirePairs = 32

0026:  // azimuthal pitch of wires (in radians)
0027:  GLOBAL dPhi       = 2*3.14159265/nWirePairs

0028:  // ======
0029:  & CELL
0030:  // ======
0031:  TUBE r={anodeR}, v={anodeV}, label=A
0032:  // cathode and cage wires
0033:  ROWS
0034:  FOR i FROM 0 TO {nWirePairs-1} DO
0035:      S * {wireD} {cathodeR*cos(i*dPhi)} {cathodeR*sin(i*dPhi)} {cathodeV}
0036:  ENDDO
0037:  FOR i FROM 0 TO {nWirePairs-1} DO
0038:      S * {wireD} {cageR*cos(i*dPhi)} {cageR*sin(i*dPhi)} {cageV}
0039:  ENDDO

0040:  // =====
0041:  & GAS
0042:  // =====
0043:  GLOBAL gasfile = 'HeCO2_90_10_250_293.gas'
0044:  GLOBAL gasmember = 'HeCO2'
0045:  CALL inquire_member(gasfile, gasmember,'gas',exist)
0046:  IF exist THEN
0047:   GET {gasfile, gasmember}
0048:  ELSE
0049:   WRITE {gasfile, gasmember}
0050:   PRESSURE 250 mbar
0051:   TEMPERATURE 293 K
0052:   MAGBOLTZ Helium-4 90 CO2 10
0053:   HEED Helium-4 90 CO2 10
0054:  ENDIF

0055:  OPT nogas-plot gas-print
```

```
0056:  >HeCO2.dat

0057:  !deact postscript
0058:  !close postscript
0059:  !del   postscript

0060:  // ======
0061:  & FIELD
0062:  // ======
0063:  !add postscript type ps_portrait file-name contourV.ps
0064:  !open postscript
0065:  !activate postscript
0066:  AREA -{anodeR} -{anodeR} +{anodeR} +{anodeR}
0067:  PLOT contour V
0068:  !deact postscript
0069:  !close postscript
0070:  !del   postscript

0071:  !add postscript type ps_portrait file-name contourV_zoom.ps
0072:  !open postscript
0073:  !activate postscript
0074:  AREA 0 0 2 2
0075:  PLOT contour V
0076:  !deact postscript
0077:  !close postscript
0078:  !del   postscript

0079:  // ======
0080:  & DRIFT
0081:  // ======
0082:  !add postscript type ps_portrait file-name tactic.ps
0083:  !open postscript
0084:  !activate postscript
0085:  AREA -{anodeR} -{anodeR} +{anodeR} +{anodeR}

0086:  // create a table of drift times for comparison
0087:  >table.dat
0088:  TABLE electron

0089:  // place electrons at a self-defined grid of points in
0090:  // one sector of the tube and calculate the time until
0091:  // they hit the anode
0092:  >arrivaltime.dat
0093:  FOR phi FROM 0 TO dPhi STEP {dPhi/10} DO
0094:    FOR r FROM cathodeR TO anodeR STEP 0.05 DO
0095:      CALL drift_electron({r*cos(phi)}, {r*sin(phi)})
0096:      CALL drift_information(‘drift-time‘,time)
0097:      //   [rad]    [cm]     [microsec]
0098:      SAY "{phi}    {r}      {time}"
0099:    ENDDO
0100:    // separate data for different phi by blank line
0101:    SAY
0102:  ENDDO

0103:  // close postscript file
0104:  !deact postscript
0105:  !close postscript
0106:  !del   postscript

0107:  & MAIN
```

Appendix C

Geant4 Simulation

C.1 Simulation Source Code

For lack of space, the source code of the GEANT4 simulation of the TACTIC chamber cannot be printed here. It is available on request. An up-to-date version is kept in the CVS repository `/home/tudacvs` on the computer `ast07.triumf.ca`.

C.2 Vertex and Angle Reconstruction

The following C++ script was employed to reconstruct the vertex point and laboratory ejection angle (see section 4.4.2). It calculates the regression line fitting the radial positions of the simulated track points. They are supplied in a three-column text file, where data from successive events are separated by a blank line.

```
0000:  #include <fstream.h>
0001:  #include <iostream.h>

0002:  int main(int argc, char** argv) {
0003:    ifstream infile(argv[1]);
0004:    const int nAnodesZ = 48;
0005:    const double driftLength = 240; // [mm]
0006:    const double anodeWidthZ = driftLength/nAnodesZ;

0007:    int currentAnode;
0008:    double r[nAnodesZ];
0009:    double delta_r[nAnodesZ];
0010:    for (int i=0; i<nAnodesZ; i++) {
0011:        r[i]       = 0;
0012         delta_r[i] = 0;
0013:    }

0014:    double z_vertex;
0015:    double delta_z_vertex;
0016:    long nEvents = 0; // number of event
0017:    long nAnodes = 0; // number of anodes affected by the event
0018:    long totalNAnodex = 0;

0019:    while (infile.good()) {
0020:      if (infile.peek() == '\n') {
0021:        // event has ended, process it
0022:        while (infile.peek() == '\n') infile.ignore(1000, '\n');

0023:        if (nAnodes > 0) {
0024:            nEvents++;
```

```
0025:            // calculate slope a and axis intercept b of regression line
0026:            // for this event
0027:            double sumx  = 0;
0028:            double sumx2 = 0;
0029:            double sumy  = 0;
0030:            double sumxy = 0;
0031:            for (int i=0; i<nAnodesZ; i++) {
0032:              if (r[i] != 0) {
0033:                    sumx  += i;
0034:                    sumx2 += i*i;
0035:                    sumy  += r[i];
0036:                    sumxy += i*r[i];
0037:              }
0038:            }
0039:            double Delta = nAnodes*sumx2 - sumx*sumx;
0040:            double a = (nAnodes*sumxy - sumx*sumy)/Delta;
0041:            double b = (sumx2*sumy - sumx*sumxy)/Delta;

0042:            // calculate and output vertex z coordinate along with number
                   of affected anodes and theta angle [deg] of regression line
0043:            z_vertex = (-b/a+0.5)*anodeWidthZ - driftLength/2.0;
0044:            double theta = atan(a/anodeWidthZ);

0045:              // for nAnodes==1 z_vertex will be NaN, since regression lines can
0046:              // only be calculated from 2 or more data points
0047:              // dirty hack to fix this:
0048:              if (nAnodes < 2) {
0049:                    z_vertex = 0;
0050:                    theta = 0;
0051:              }
0052:              // REMEMBER NOT TO USE THESE VALUES at the time of averaging!!!

0053:              cout << nAnodes << "   " << z_vertex << "   " << theta << endl;
0054:          }

0055:          // empty transient variables for next event
0056:          nAnodes = 0;
0057:          for (int i=0; i<nAnodesZ; i++) {
0058:              r[i]       = 0;
0059:              delta_r[i] = 0;
0060:          }
0061:       } else {
0062:          // read event data
0063:          infile >> currentAnode;
0064:          infile >> r[currentAnode];
0065:          infile >> delta_r[currentAnode];
0066:          infile.ignore(1000, '\n');
0067:          nAnodes++;
0068:       }
0069:     }
0070:     return 0;
0071:  }
```

Bibliography

[1] C.E. Rolfs, and W.S. Rodney: *Cauldrons in the Cosmos*, The University of Chicago Press, 1988

[2] T. Mayer-Kuckuck, *Kernphysik*, 4th edition, Teubner, 1984

[3] D.G. Gigliotti, Master thesis, University of Northern British Columbia, Canada, 2004

[4] S. Engel, Dissertation, Ruhr-Universität Bochum, Germany, 2003

[5] A.M. Baldin, *Kinematics of Nuclear Reactions*, Pergamon Press, 1961

[6] G. Ruprecht, TRIUMF, Private Communication

[7] P. Walden, A.M. Laird, *A study of the partial and total cross sections of the* $^{8}Li(\alpha,n)^{11}B$ *reaction at astrophysically relevant energies*, TRIUMF Research Proposal E964, `http://tuda.triumf.ca/proposals_appr/E964/E964.pdf`

[8] T. Hashimoto *et al.*, Nucl. Phys. A **746** (2004) 330c-334c

[9] M. Terasawa *et al.*, Astr. J. **562** (2001) 470-479

[10] `http://www.triumf.ca`

[11] G. Ruprecht, D. Gigliotti, P. Amaudruz, L. Buchmann, S.P. Fox, B.R. Fulton, T. Kirchner, A.M. Laird, P.D. Mumby-Croft, R. Openshaw, M.M. Pavan, J. Pearson, G. Sheffer, and P. Walden: *Status of the TRIUMF Annular Chamber for the Tracking and Identification of Charged Particles (TACTIC)*, submitted to Eur. Phys. J. - available on request

[12] `http://tactic.triumf.ca`

[13] Y. Mizoi *et al.*, Nucl. Instr. and Meth. in Phys. Res. A, **431** (1999) 112-122

[14] F. Sauli, Nucl. Instr. and Meth. in Phys. Res. A, **386** (1997) 531-534

[15] `http://midas.triumf.ca`

[16] `http://midas.psi.ch/rome`

[17] `http://root.cern.ch`

[18] L. Buchmann, $^{7}Be+p$*: elastic scattering*, TRIUMF Research Proposal, `http://tuda.triumf.ca/internal/proposals_subm/7Be_final.pdf`

[19] http://www.triumf.ca/isac/isac_home.html

[20] http://dragon.triumf.ca

[21] http://tuda.triumf.ca

[22] G. Ruprecht: *Report: GEM pressure investigations*, TRIUMF, March 2005 - available on request

[23] FEMLAB User Guide, COMSOL Inc., 2004

[24] http://www.comsol.com/products/femlab

[25] A. Peisert, and F. Sauli, *Drift and Diffusion of Electrons in Gases: A Compilation*, CERN 84-08, 1984

[26] http://garfield.web.cern.ch/garfield

[27] http://consult.cern.ch/writeup/magboltz

[28] http://geant4.web.cern.ch/geant4

[29] S. Agostinelli *et al.*, Nucl. Instr. and Meth. in Phys. Res. A, **506** (2003) 250-303

[30] GEANT4 User's Guide for Application Developers, http://geant4.web.cern.ch/geant4/G4UsersDocuments/UsersGuides/ForApplicationDeveloper/html/index.html

[31] V.N. Ivanchenko *et al.*, CERN-99-121, September 1999

[32] V.N. Ivanchenko *et al.*, CERN-99-300, November 1999

[33] GEANT4 Physics Reference Manual, Version 7.0, December 2004, http://geant4.web.cern.ch/geant4/G4UsersDocuments/UsersGuides/PhysicsReferenceManual/print/PhysicsReferenceManual70.pdf

[34] B.-U. Runge, *Physikalisches Anfängerpraktikum*, Universität Konstanz, http://ap.physik.uni-konstanz.de, June 2005

[35] http://www.srim.org